An Integrated Model of Cardiac Mitochondrial Energy Metabolism and Calcium Dynamics

Sonia Cortassa,* Miguel A. Aon,* Eduardo Marbán,*† Raimond L. Winslow,†* and Brian O'Rourke*
The Johns Hopkins University, *Institute of Molecular Cardiobiology and †The Center for Computational Medicine and Biology, Baltimore, Maryland

ABSTRACT We present an integrated thermokinetic model describing control of cardiac mitochondrial bioenergetics. The model describes the tricarboxylic acid (TCA) cycle, oxidative phosphorylation, and mitochondrial Ca^{2+} handling. The kinetic component of the model includes effectors of the TCA cycle enzymes regulating production of NADH and $FADH_2$, which in turn are used by the electron transport chain to establish a proton motive force ($\Delta\mu_H$), driving the F_1F_0-ATPase. In addition, mitochondrial matrix Ca^{2+}, determined by Ca^{2+} uniporter and Na^+/Ca^{2+} exchanger activities, regulates activity of the TCA cycle enzymes isocitrate dehydrogenase and α-ketoglutarate dehydrogenase. The model is described by twelve ordinary differential equations for the time rate of change of mitochondrial membrane potential ($\Delta\Psi_m$), and matrix concentrations of Ca^{2+}, NADH, ADP, and TCA cycle intermediates. The model is used to predict the response of mitochondria to changes in substrate delivery, metabolic inhibition, the rate of adenine nucleotide exchange, and Ca^{2+}. The model is able to reproduce, qualitatively and semiquantitatively, experimental data concerning mitochondrial bioenergetics, Ca^{2+} dynamics, and respiratory control. Significant increases in oxygen consumption (V_{O_2}), proton efflux, NADH, and ATP synthesis, in response to an increase in cytoplasmic Ca^{2+}, are obtained when the Ca^{2+}-sensitive dehydrogenases are the main rate-controlling steps of respiratory flux. These responses diminished when control is shifted downstream (e.g., the respiratory chain or adenine nucleotide translocator). The time-dependent behavior of the model, under conditions simulating an increase in workload, closely reproduces experimentally observed mitochondrial NADH dynamics in heart trabeculae subjected to changes in pacing frequency. The steady-state and time-dependent behavior of the model support the hypothesis that mitochondrial matrix Ca^{2+} plays an important role in matching energy supply with demand in cardiac myocytes.

INTRODUCTION

The high metabolic demand of the heart necessitates close matching of energy production to workload. Approximately 2% of cellular ATP is consumed on each heartbeat and almost all of this energy is replenished by mitochondrial oxidative phosphorylation under normoxic conditions (Harris and Das, 1991). Remarkably, the vital process of control and regulation of mitochondrial metabolism is not well understood.

After the development of the chemiosmotic theory of energy transduction by Mitchell (1961), several hypotheses for control of metabolism have been proposed. The first, referred to as respiratory control (Chance and Williams, 1956; Harris and Das, 1991), asserts that ADP availability to the ATP synthase is the limiting factor for mitochondrial ATP production. Increases in workload lead to a rise in cellular ADP and stimulation of oxidative phosphorylation, with the downstream ''pull'' on electron transport eventually causing acceleration of NADH production by the TCA cycle. The lack of a substantial increase in whole-heart ADP concentration in response to increased pacing frequency, and the observed decrease in $\Delta\mu_H$ produced by Ca^{2+} entry into mitochondria (Heineman and Balaban, 1990; Territo et al., 2000), have been used to argue against activation of ATP synthase based solely on its substrates (Harris and Das, 1991).

A second control hypothesis emerged from the discovery that Ca^{2+} activates mitochondrial matrix dehydrogenases (McCormack and Denton, 1984; McCormack et al., 1990). According to this hypothesis an increase in the workload of the heart is accompanied by a rise in cytosolic Ca^{2+}, and the subsequent effect of matrix Ca^{2+} on the TCA cycle increases the supply of reducing equivalents (NADH, $FADH_2$) and an increased ''push'' of electrons through the respiratory chain, thereby increasing ATP production by generating more proton motive force. However, it has been argued that dehydrogenase activation by Ca^{2+} might not account quantitatively for observed changes in ATP synthesis rates (Harris and Das, 1991). Therefore, additional regulatory mechanism(s), including direct activation of the ATP synthase by Ca^{2+} (Territo et al., 2000), have been hypothesized to explain the acceleration of ATP production (Heineman and Balaban, 1990, Harris and Das, 1991). The present work addresses the hypothesis that Ca^{2+} is involved in coupling energy demand and supply in heart mitochondria. This hypothesis is tested through development and application of an integrative mathematical model that takes into account mitochondrial matrix- and membrane-based processes such as the TCA cycle, oxidative phosphorylation, and Ca^{2+} dynamics. To date, an integrated kinetic and thermodynamic model of cardiac energy metabolism

Submitted February 13, 2002, and accepted for publication November 26, 2002.

Address reprint requests to Brian O'Rourke, Ph.D., The Johns Hopkins University, Institute of Molecular Cardiobiology, 720 Rutland Ave., 844 Ross Bldg., Baltimore, MD 21205-2195. Tel.: 410-614-0034; Fax: 410-955-7953; e-mail: bor@jhmi.edu.

0006-3495/03/04/2734/22 $2.00

incorporating mitochondrial Ca^{2+} dynamics has not been available. The present work builds a unified model of mitochondrial energy metabolism and examines its behavior with respect to changes in substrate supply, metabolic inhibition, and Ca^{2+}. The results provide insight into the essential control properties of the system.

METHODS

General description

The model incorporates the main mitochondrial electrophysiological and metabolic processes and their interactions (Fig. 1). Model differential equations are given in Table 1, whereas rate equations and their behavior are presented in the Appendix. The major components of the model—mitochondrial matrix-associated processes, oxidative phosphorylation, and Ca^{2+} dynamics—are described in the following sections.

Mitochondrial matrix-associated processes

The tricarboxylic acid (TCA) cycle

The first phase of the model, the TCA cycle, represents the end stage for carbon substrates in the cell. The catabolic pathways for substrate oxidation (e.g., fatty acids, amino acids, and sugars) converge to produce AcCoA, the main input of the TCA cycle.

The dashed lines in Fig. 1 show the regulatory feedback loops incorporated into the model. The rates of the highly-regulated dehydro-

TABLE 1 Model differential equations

State variable	Differential equation	
$[ADP]_m$	$\frac{d[ADP]_m}{dt} = V_{ANT} - V_{ATPase} - V_{SL}$	(1)
$\Delta\Psi_m$	$\frac{d\Delta\Psi_m}{dt} = \frac{V_{He}+V_{He(F)} - V_{Hu} - V_{ANT} - V_{HLeak} - V_{NaCa} - 2V_{uni}}{C_{mito}}$	(2)
[NADH]	$\frac{d[NADH]}{dt} = -V_{O_2} + V_{IDH} + V_{KGDH} + V_{MDH}$	(3)
[ISOC]	$\frac{d[ISOC]}{dt} = V_{ACO} - V_{IDH}$	(4)
[αKG]	$\frac{d[\alpha KG]}{dt} = V_{IDH} - V_{KGDH} + V_{AAT}$	(5)
[SCoA]	$\frac{d[SCoA]}{dt} = V_{KGDH} - V_{SL}$	(6)
[Suc]	$\frac{d[Suc]}{dt} = V_{SL} - V_{SDH}$	(7)
[FUM]	$\frac{d[FUM]}{dt} = V_{SDH} - V_{FH}$	(8)
[MAL]	$\frac{d[MAL]}{dt} = V_{FH} - V_{MDH}$	(9)
[OAA]	$\frac{d[OAA]}{dt} = V_{MDH} - V_{CS} - V_{AAT}$	(10)
[ASP]	$\frac{d[ASP]}{dt} = V_{AAT} - V_{C\_ASP}$	(11)
$[Ca^{2+}]_m$	$\frac{d[Ca^{2+}]_m}{dt} = f(V_{uni} - V_{NaCa})$	(12)

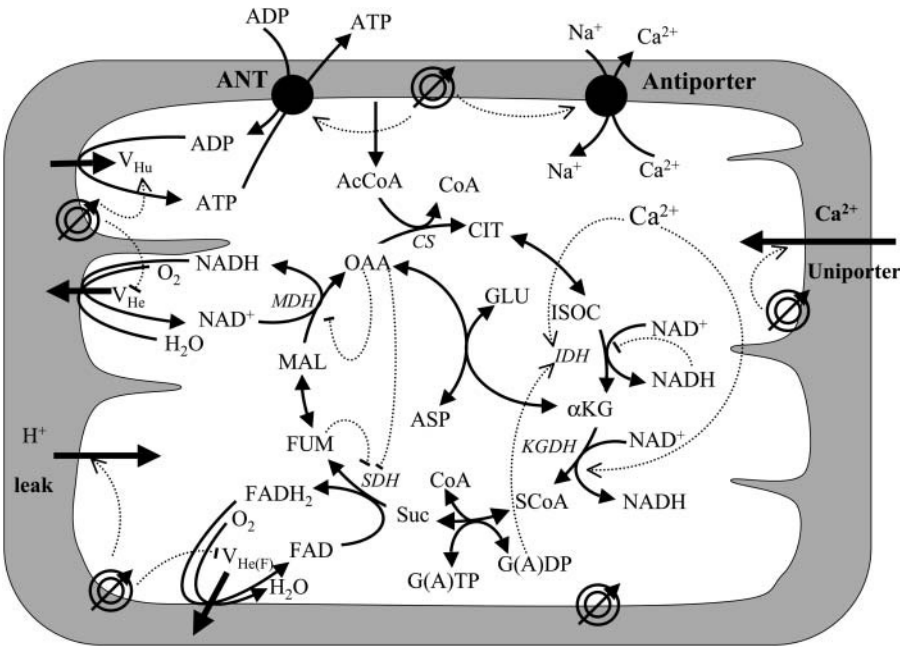

FIGURE 1 Schematic representation of the mitochondrial electrophysiological and metabolic processes and their interactions, as described by the model. The model takes into account oxidative phosphorylation and matrix-based processes in mitochondria. The tricarboxylic (TCA) cycle of the mitochondrial matrix is fed by acetyl CoA (AcCoA), which is the point of convergence for the oxidation of fatty acids and glucose, the two main substrates of the heart. The TCA (or Krebs) cycle completes the oxidation of AcCoA to CO_2 and produces NADH and $FADH_2$, which provide the driving force for oxidative phosphorylation. NADH and $FADH_2$ are oxidized by the respiratory chain and the concomitant pumping of protons across the mitochondrial inner membrane establishes an electrochemical gradient, or proton motive force ($\Delta\mu_H$), composed of an electrical gradient ($\Delta\Psi_m$) and a proton gradient (ΔpH). This proton motive force drives the phosphorylation of matrix ADP to ATP by the F_1F_0-ATPase (ATP synthase). The large $\Delta\Psi_m$ of the inner membrane (-150 to -200 mV; matrix negative with respect to the cytoplasm) also governs the electrogenic transport of ions, including the cotransport of ATP and ADP by the adenine nucleotide translocator, Ca^{2+} influx via the Ca^{2+} uniporter and Ca^{2+} efflux via the Na^+/Ca^{2+} antiporter (Magnus and Keizer, 1997). The model also accounts for the explicit dependence of the TCA cycle enzymes isocitrate dehydrogenase and α-ketoglutarate dehydrogenase on Ca^{2+}. In this way, the rate of Ca^{2+} uptake by mitochondria is involved in membrane energization through the TCA cycle and oxidative phosphorylation, which are described in detail in the Appendix. Key to symbols: The concentric circles with an arrow across located at the inner mitochondrial membrane represent the $\Delta\Psi_m$. Dotted arrows indicate regulatory interactions either positive (*arrowhead*) or negative ($-$).

genases of the TCA cycle, namely, citrate synthase (CS), isocitrate dehydrogenase (IDH), α-ketoglutarate dehydrogenase (KGDH) and malate dehydrogenase (MDH) and their regulatory interactions have been studied in detail and their behavior is presented in the Appendix. A fundamental feature of the present model is the explicit dependence of the dehydrogenases IDH and KGDH on mitochondrial calcium (Rutter and Denton, 1988; McCormack and Denton, 1984; Nichols et al., 1994; McCormack et al., 1990; Hansford and Zorov, 1998; also see Appendix).

Oxidative phosphorylation (OxPhos)

The OxPhos model is based on that of Magnus and Keizer (1997). The model describes NADH-driven electron transport and proton efflux, and F_1F_0-ATPase activity and its associated proton influx (Fig. 1; see also Appendix). The adenine nucleotide translocator and the proton leak are also taken into account. In general, this model follows a thermokinetic formulation. The driving forces are redox (A_{res}) and phosphorylation (A_{F1}) potentials (see Eqs. 26–34) and the proton motive force ($\Delta\mu_H$). Coefficients in the equations correspond to rate constants of explicit conversion steps postulated in the Altman-King-Hill formulation of the model (Pietrobon and Caplan, 1985; Magnus and Keizer, 1997).

The F_1F_0-ATPase

The original expression for the rate of the F_1F_0-ATPase (Magnus and Keizer, 1997) was modified to account for reversibility of the enzyme when $\Delta\mu_H$ collapses (see Appendix). For example, in uncoupled mitochondria, hydrolysis rather than synthesis of ATP can occur and drive proton pumping.

Mitochondrial calcium dynamics

Mitochondrial Ca^{2+}, $[Ca^{2+}]_m$, is determined mainly by Ca^{2+} influx through the Ca^{2+} uniporter and the Na^+-dependent Ca^{2+} efflux driven by the Na^+/Ca^{2+} antiporter. The latter is assumed to be electrogenic based on the reported results of Baysal et al. (1994) (see Appendix).

Model building and numerical methods

The model was built using a modular approach. Briefly, each model component was examined separately, iteratively fine-tuning the kinetic parameters for the best fit to experimental data (Eqs. 13–39). Maple (Maple V, release 4, Waterloo, Canada) was used to study each analytical expression as a function of underlying parameters (see electronic Appendix: http://www.jhmi.edu/bor/model.htm).

Before the final model assembly, the TCA cycle and OxPhos modules were analyzed separately. The adequacy of the expressions for each of the processes involved was tested by simulating the model behavior at steady state. The system was considered to be in steady state when the magnitude of each time derivative was $\leq 10^{-13}$. Model parameters such as the level of AcCoA, ion leak, and levels of electron carriers, were then varied to determine their influence on important mitochondrial functions. If the results were counterintuitive, or inconsistent with basic bioenergetic principles, the model was revised at the level of the analytical expressions stated in Maple and retested. The iteration process was performed until complete and satisfactory expressions were obtained, which converged to results consistent with available experimental evidence.

Numerical integration of model equations (Eqs. 1–12, Table 1) was performed using an Adams routine (SCoP, version 3.51w, Simulation Resources) until steady-state solutions (according to the criterion described above) were obtained. Steady-state values of each state variable were then used as input to software for performing bifurcation and continuation analysis (AUTO 1997, E. Doedel, Concordia University). This software was used to determine the dependence of steady-state solution properties (type and stability) on model parameters.

Dynamic simulations

To test whether or not the global kinetic response of the model accurately reproduces the dynamic response of mitochondrial energetics to changes in workload, we simulated the time-dependent behavior of mitochondrial NADH and Ca^{2+} during changes in the myocardial pacing frequency. Forcing pulse functions (SCoP version 3.51w, Simulation Resources) for the parameters $[Ca^{2+}]_i$ and $[ADP]_i$ were incorporated into the model, and the simulations were compared with experimental data obtained in cardiac trabeculae (Brandes and Bers, 2002). Ca^{2+} transients were simulated with periodic square pulses of $[Ca^{2+}]_i$ to 1 μM (from a basal level of 100 nM) for 400 ms duration, applied at frequencies of 0.25 Hz or 2 Hz. To simulate the increased energy consumption when pacing frequency was increased, a single $[ADP]_i$ pulse from 50 to 150 μM was applied for the whole interval of high frequency stimulation.

RESULTS

Simulations of the response of mitochondrial energetics to changes in substrate input, levels of electron carriers, and cytoplasmic Ca^{2+} were performed to test whether the model qualitatively and semiquantitatively reproduced available experimental evidence. The overriding objective was to gain insight into the important sites and mechanisms of control of bioenergetics.

Control properties of the integrated model

Metabolic control analysis of oxidative phosphorylation has previously been used to demonstrate that control is distributed among the respiratory chain/substrate transport, the phosphorylation system, and the proton leak (Hafner et al., 1990; Murphy, 2001). This control can redistribute during electron chain inhibition, mitochondrial uncoupling, or with postischemic mitochondrial damage (Borutaite et al., 1995). Therefore, the simulations presented below examine the effects of metabolic perturbation on mitochondrial energetics to better understand control of the integrated system (Brand and Kesseler, 1995).

Influence of AcCoA on mitochondrial energetics

The contribution of substrate availability to the global response of bioenergetics was tested by varying either the earliest (AcCoA) or last (ADP) substrate (next section) of the integrated model. When the concentration of AcCoA was increased to a maximum of 10 μM, an approximate twofold increase in V_{O_2} was obtained; beyond this, V_{O_2} plateaued (Fig. 2 *A*). This increase in respiration rate is driven by the generation of NADH in the range of 0.001–1.5 mM (Fig. 2 *A*). The V_{O_2} registered at very low AcCoA is mainly driven by glutamate (see Appendix Eq. 24).

Over the full range of the V_{O_2} increase, stimulation of electron transport is associated with a modest increase in $\Delta\Psi_m$ ($\sim$14 mV; Fig. 2 *B*). The linear flow-force relationship

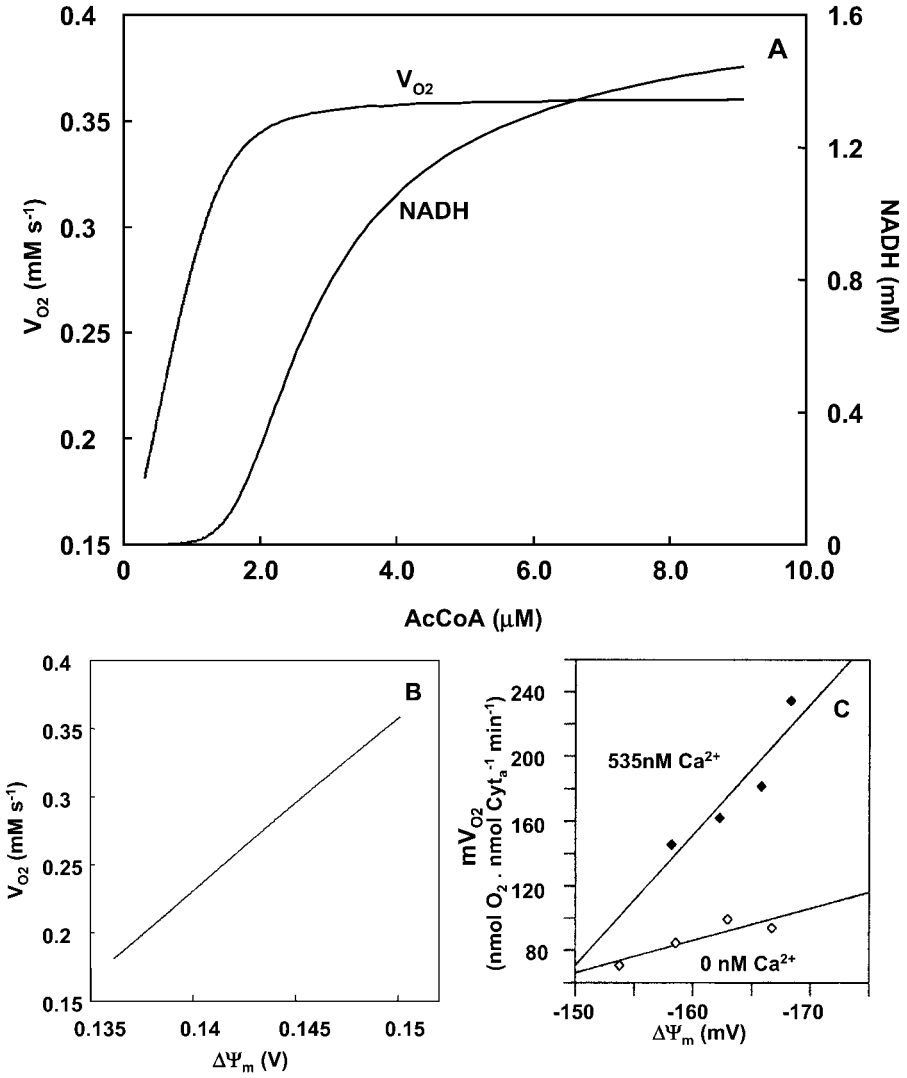

FIGURE 2 Effects of increasing substrate delivery on mitochondrial energetics. AcCoA concentration is varied and the steady-state behavior of the model analyzed according to a continuation analysis (see text). The correlative changes in the steady-state behavior of V_{O_2} and NADH versus (*A*) AcCoA and (*B*) $\Delta\Psi_m$ are depicted when AcCoA is systematically changed. The simulation was run with the following set of parameters: $V_{maxANT} = 5.0$ mM s^{-1}; $\Delta pH = -0.6$; $\rho^{res} = 0.048$ mM; ADPi $= 0.05$ mM; $V_{max}^{NaCa} = 0.05$ mM s^{-1}; $\rho^{F1} = 0.06$ mM; $[Ca^{2+}]_i = 0.5$ μM; $g_H = 0.01$ mM s^{-1} V^{-1}. The rest of the parameters are as indicated in Table 3. (*C*) Simulation results match experimental data obtained with pig heart mitochondria, redrawn from Territo et al. (2000).

between V_{O_2} and $\Delta\Psi_m$ represented in Fig. 2 *B* is in agreement with experimental results reported for cardiac mitochondria by Territo et al. (2000) (redrawn in Fig. 2 *C*).

Influence of phosphorylation potential on mitochondrial energetics

The respiratory rate (V_{O_2}) increases as a function of the maximal rate of the adenine nucleotide translocator, ANT (Fig. 3 *A*) by ~six-to-sevenfold before saturation. In keeping with the classical theory of respiratory control, V_{O_2} varies with matrix ADP concentrations in the mM range (Fig. 3 *A*, *inset*). At low ADP, representing state 4 respiration, the basal rate of oxygen consumption is nonzero, supported in the model by a small proton leak across the mitochondrial inner membrane. A steep response of V_{O_2} to small changes in ADP, as would occur during increased metabolic demand, is evident as the transition is made from state 4 to state 3.

At this point it is worthwhile introducing the definition of "push" or "pull" conditions as those in which the control exerted on the respiratory flux correspond to processes upstream (e.g., TCA cycle) or downstream (e.g., ANT, respiration, ATPase) of NADH, respectively (see also Metabolic Control Analysis of Mitochondrial Energetics). Push is obtained when simulations are performed with a large concentration of respiratory electron carriers, ρ^{RES}, and low k_{cat} for both IDH and KGDH activities, whereas the opposite is true for pull conditions (see Fig. 5 legend). A decline in $\Delta\Psi_m$ accompanies ADP stimulation of V_{O_2} under pull conditions (Fig. 3 *B*). Thus, respiration is stimulated as phosphorylation potential drops along with an increased F_1F_0ATPase activity.

Conditions which diminish the ability of the respiratory chain to oxidize NADH decrease V_{O_2} for any given ADP concentration (Fig. 3, *A* and *B*, *trace a*). This is simulated by decreasing the maximum velocity of the ANT, and reducing the concentration of respiratory electron carriers (ρ^{res}) by sevenfold.

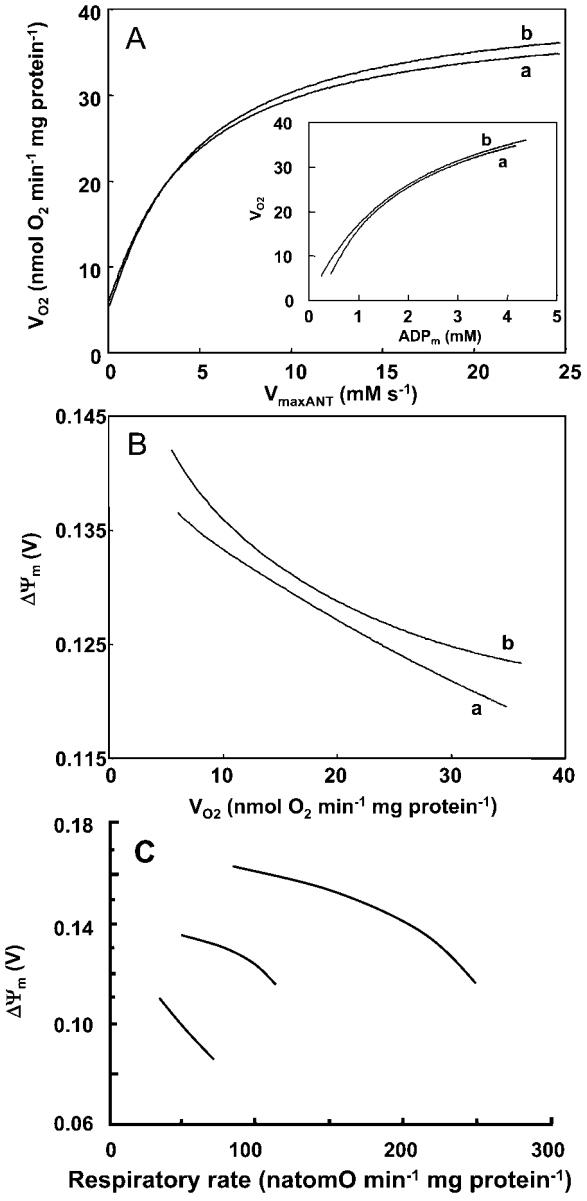

FIGURE 3 Relationship between membrane potential and respiratory flux upon changes in adenine nucleotide translocator activity. The changes in respiration rate, V_{O_2}, and membrane potential, $\Delta\Psi_m$, are determined by the behavior of the whole model according to a steady-state analysis performed at different adenine nucleotide translocator maximal activities (V_{maxANT}) which result in different ADP_m concentrations (*A*, *inset*). The left portion of curves *a* and *b* in panels *A* and *B*, corresponds to mitochondria in state 4 (i.e., low ADP) and the increases in V_{O_2} result from the respiratory control exerted by increasing ADP concentrations. The simulations were run with the following parameter values: (*a*) $\Delta pH = -0.6$; $\rho^{res} = 0.00072$ mM; $ADP_i = 0.05$ mM; $V_{max}^{NaCa} = 0.05$ mM s^{-1}; $\rho^{F1} = 1.216$ mM; $[Ca^{2+}]_i = 0.1$ μM; $g_H = 0.01$ mM s^{-1} V^{-1}; AcCoA = 1.0 mM. V_{maxANT} is varied in the range 0.01–25 mM s^{-1}; (*b*) all parameters are the same as in *a*, except for $\rho^{res} = 0.0051$ mM and $\rho^{F1} = 0.61$ mM. The remainder of the parameters are reported in Table 3. (*C*) Changes in the relationship between $\Delta\Psi_m$ and the respiratory rate obtained at various ratios of creatine/creatine phosphate in a preparation of heart mitochondria with normal or reduced respiratory activity (*left-shifted curves*). Redrawn from Borutaite et al. (1995).

The results in Fig. 3 *B* are in qualitative agreement with the experimental results obtained with isolated heart mitochondria (reproduced in Fig. 3 *C*; Borutaite et al., 1995). Under conditions of a decrease in the respiratory activity of heart mitochondria due to ischemia, the curve describing the relation between $\Delta\Psi_m$ and succinate-driven respiratory rate is shifted down and to the left with respect to the behavior of normal mitochondria (Fig. 3 *C*).

Influence of proton leak and respiratory inhibition on mitochondrial energetics

Inhibition of respiration is simulated by decreasing the concentration of electron carriers in the mitochondrial membrane (ρ^{res}) (Fig. 4 *A*). The steepness of the V_{O_2} curve over the low range of ρ^{res}, and the electron carrier concentration at which V_{O_2} reaches saturation, are influenced by the magnitude of proton influx across the inner membrane, as depicted in Fig. 4 *A*, curves *a* and *b*. Proton influx can be varied by changing the concentration of F_1F_0-ATPase, which dissipates $\Delta\mu_H$. Increasing the concentration of F_1F_0-ATPase increases V_{O_2} over the low ρ^{res} range (Fig. 4 *A*; *curve a*). As expected, with minimal ATP synthase activity, the membrane can support a higher $\Delta\Psi_m$ at any V_{O_2} (Fig. 4 *B*; *curve b*). These modeling results resemble experimental data obtained with normal mitochondria in either state 3 or 4 upon titration with the metabolic inhibitor malonate at various creatine/creatine phosphate ratios (Fig. 4 *C*; Borutaite et al., 1995).

Response of mitochondrial energetics to changes in cytoplasmic and mitochondrial Ca^{2+}

There are two effects of Ca^{2+} on mitochondrial bioenergetics that are diametrically opposed: on the one hand, Ca^{2+} influx dissipates $\Delta\Psi_m$ and decreases the proton motive force; on the other, Ca^{2+} stimulates the production of NADH by the TCA cycle, increasing the proton motive force and ATP production. One of the main objectives of this study is to determine the balance between these effects under different conditions. Therefore, simulations are presented using two different parameter sets that illustrate different model behaviors. A key question is whether or not the intrinsic biophysical properties of the system allow control of mitochondrial metabolism by matrix Ca^{2+}.

Steady-state behavior of mitochondrial calcium

The first step toward understanding the effects of Ca^{2+} on the global behavior of the model is to simulate the steady-state response of mitochondrial matrix free Ca^{2+} ($[Ca^{2+}]_m$) to changes in free cytosolic Ca^{2+} concentration ($[Ca^{2+}]_i$). Inasmuch as there is little quantitative information about the relative contributions of the two major Ca^{2+} transport pathways in determining steady-state $[Ca^{2+}]_m$, the parameter

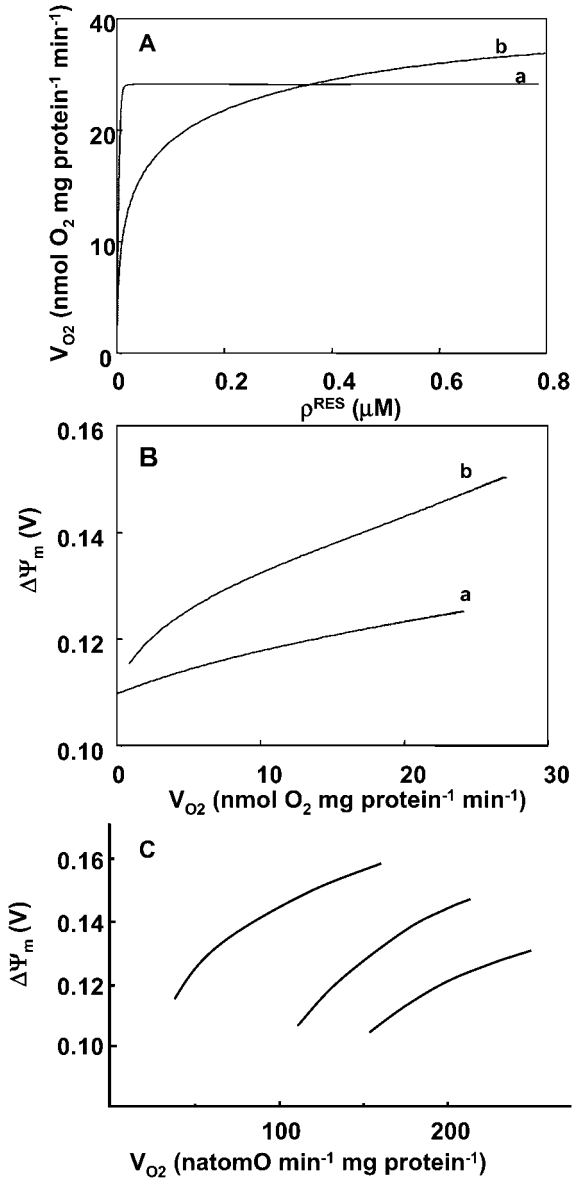

FIGURE 4 Relationship between mitochondrial inner membrane potential and the respiratory flux. The rate of the electron transport chain and the $\Delta\Psi_m$ are modulated through the concentration of electron carriers (ρ^{res}) (*A*, *B*). A steady-state analysis of the whole model behavior is performed. The parameters utilized in the simulations are those reported in Table 3 and as follows: $P_i = 20.0$ mM; $\Delta pH = -0.6$; $V_{maxANT} = 5.0$ mM s^{-1}; $ADP_i = 0.05$ mM; $V_{max}^{NaCa} = 0.05$ mM s^{-1}; $g_H = 0.01$ mM s^{-1} V^{-1}, $[Ca^{2+}]_i = 0.1$ μM and AcCoA = 1.0 mM. The values of F_1F_0-ATPase concentration, ρ^{F1}, differ between curves, being 1.216 mM for curve *a* and 0.06 mM for curve *b*. (*C*) Changes in the relationship between $\Delta\Psi_m$ and the respiratory rate obtained upon malonate titration at different phosphorylation potentials (different ratios of creatine to creatine phosphate) in a preparation of heart mitochondria. Redrawn from Borutaite et al. (1995).

space is explored with respect to the maximal Na^+/Ca^{2+} antiporter rate. Results of these studies show that following $[Ca^{2+}]_i$ changes in the physiological range (0.01 to 1.2 μM), $[Ca^{2+}]_m$ increases nonlinearly after crossing a certain threshold $[Ca^{2+}]_i$, and continues to increase to more than 20 μM without saturation (Fig. 5 *A*). This threshold depends on the ratio of Ca^{2+} uniporter and Na^+/Ca^{2+} antiporter rates. In fact, the rightward shift of the $[Ca^{2+}]_m$ curve (Fig. 5, trace *a*) is due to a large increase in the rate of the Na^+/Ca^{2+} antiporter, which counteracts influx through the Ca^{2+} uniporter. The general profile of $[Ca^{2+}]_m$ accumulation upon increasing $[Ca^{2+}]_i$ are in agreement with experimental results obtained by several authors (Fig. 5 *B*) (Miyata et al., 1991; Collins et al., 2001; reviewed by McCormack et al., 1990). The right shift in the experimental curve shown in Fig. 5 *B* was elicited by the addition of Na^+ (McCormack et al., 1990) supporting the involvement of the Na^+/Ca^{2+} antiporter in this response.

As the rates of the Ca^{2+} uniporter and Na^+/Ca^{2+} antiporter are coupled indirectly through $\Delta\Psi_m$, the steady-state $[Ca^{2+}]_m$ uptake curve (Fig. 5 *A*) is relatively unaltered by changing other parameters that determine push or pull conditions. The

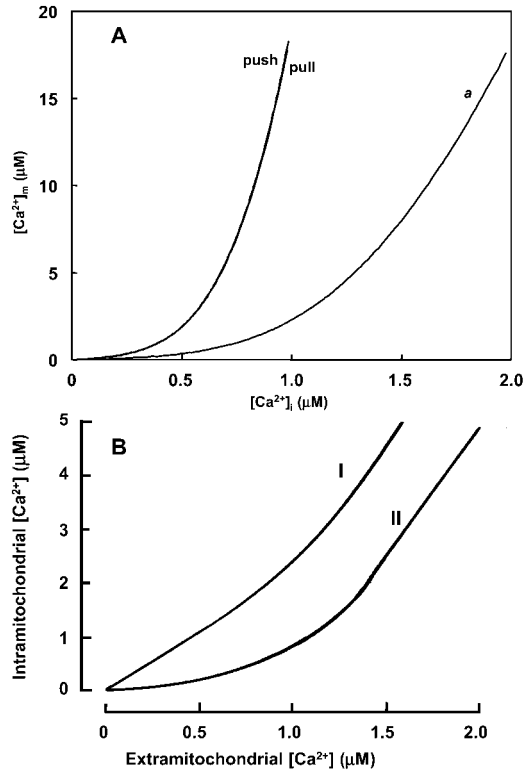

FIGURE 5 Mitochondrial Ca^{2+} level after changes in cytoplasmic Ca^{2+}. (*A*) The behavior of the whole model is studied with the AUTO 97 software as a function of cytoplasmic Ca^{2+} concentration, $[Ca^{2+}]_i$. The simulations were performed with the following set of parameters: (*pull*): $\rho^{RES} = 0.00072$ mM, $\rho^{F1} = 1.216$ mM, $k_{cat}^{IDH} = 16.3$ s^{-1}, $k_{cat}^{KGDH} = 5.0$ s^{-1}, and $V_{max}^{NaCa} = 0.005$ mM s^{-1}, and (*push*): $\rho^{RES} = 0.0036$ mM, $\rho^{F1} = 0.0522$ mM, $k_{cat}^{IDH} = 1.94$ s^{-1}, $k_{cat}^{KGDH} = 0.15$ s^{-1}, and $V_{max}^{NaCa} = 0.005$ mM s^{-1}. Curve *a* is obtained with the same parametric set as "pull" except for $V_{max}^{NaCa} = 0.05$ mM s^{-1}. Otherwise the concentration of AcCoA is 1.0 mM, and the catalytic constants of CS and MDH are $k_{cat}^{CS} = 3.2$ s^{-1} and $k_{cat}^{MDH} = 27.75$ s^{-1}, respectively. (*B*) Experimental results redrawn from McCormack et al. (1990) showing the accumulation of mitochondrial Ca^{2+} in the absence (*curve I*) or in the presence of Na^+ (*curve II*).

effect of $[Ca^{2+}]_i$ on V_{O_2}, however, is sensitive to such parameters, as described in the following section.

Response of mitochondrial energetics to changes in Ca^{2+}

Effects on V_{O_2}

Activation of V_{O_2} by Ca^{2+} is evident for both push and pull parameter sets (Fig. 6 *A*). Higher basal V_{O_2} values at a given $[Ca^{2+}]_i$ are evident for conditions in which the ANT and the electron transport flux are the main rate-controlling steps of respiration (pull) (Table 2). However, the degree of activation by Ca^{2+} is reduced compared to the push condition (~9.1% versus 23%, Fig. 6 *A*) due to the Ca^{2+} insensitivity of the main rate-controlling steps of respiration. Paralleling the increase in V_{O_2}, the steady-state fluxes through the Ca^{2+}-sensitive enzymes, KGDH and IDH, also increases as a function of Ca^{2+} (Fig. 6 *B*, *inset*).

Effects on NADH and $\Delta\Psi_m$

A positive correlation between NADH and Ca^{2+} was obtained for the pull condition and the intermediate Ca^{2+} range for push (Fig. 6 *B*). Similar to the behavior of V_{O_2}, higher levels of NADH are obtained when the control shifts toward the respiratory chain (pull) (Fig. 6 *B*). However, this condition gives a relatively smaller stimulation of NADH by Ca^{2+} (1.8-fold against 3.7-fold over the same range of $[Ca^{2+}]_i$) (Fig. 6 *B*). For the push condition, $\Delta\Psi_m$ is slightly increased with an increase in Ca^{2+} (Fig. 7 *B*)—this is possible only if the stimulatory effect of Ca^{2+} on TCA cycle, and the concomitant increase in proton pumping, exceed the depolarization of $\Delta\Psi_m$ due to energy dissipation by Ca^{2+} entry. The decrease in NADH observed at high $[Ca^{2+}]_i$ in the push condition is due to saturation of the stimulatory effect on dehydrogenase activity whereas respiratory flux continues to increase (Fig. 6, *A* and *B*, *inset*).

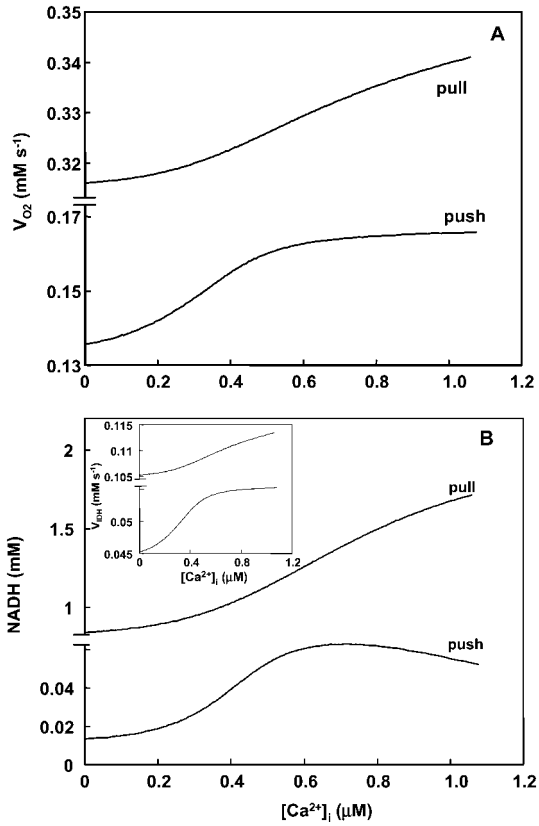

FIGURE 6 Respiratory flux and NADH levels upon changes in $[Ca^{2+}]_I$. The model is analyzed as described in Fig. 5 with the same set of parameters indicated in its legend for push and pull conditions. The steady-state respiratory flux (*A*) and NADH concentration (*B*) corresponding to the same simulations presented in Fig. 5 are depicted as a function of $[Ca^{2+}]_i$.

TABLE 2 Control of the respiratory flux by TCA cycle enzymes and the rates of membrane-associated processes

	Parametric set, flux control coefficient	
	Push	Pull
TCA cycle		
CS	0.33	0.35
IDH	22.8	5.3
KGDH	70.0	0.3
MDH	3.6	13.9
Membrane-associated processes		
ANT	3.8	38
Respiration	2.1	6.7
F_1F_0-ATPase	−0.2	2.7
Proton leak	0.1	0.3

The control exerted by the rate of each process on mitochondrial respiration is quantified around the steady state corresponding to the set of parameters indicated in the legend of Fig. 5. The flux control coefficient (in %) indicates to which extent a flux (i.e., the respiratory flux) changes upon a change on the activity of an enzyme in the pathway. The flux control coefficient was calculated from the slope of the double logarithmic plot of V_{O_2} as a function of the process rate under study. Under push and pull conditions, the flux control coefficients were determined at a $[Ca^{2+}]_i$ concentration of 0.1 or 0.5 μM. Inasmuch as the differences between flux control coefficients quantified at 0.1 or 0.5 μM are 1% or less, we present the data obtained with 0.1 μM.

In the cases of CS, IDH, KGDH, and MDH the k_{cat} is varied around the steady-state level (<5% change) to compute the control coefficient. ρ^{res} and ρ^{F1} are varied (<10% change) to compute the control exerted by respiration itself and the F_1F_0-ATP synthase, respectively. The control exerted by the adenine nucleotide translocator and the proton leak is performed with parameters V_{maxANT} and g_H, respectively.

Effects on V_{ATPase}

The fundamental question of whether the sum total of the effects of Ca^{2+} on bioenergetics is able to increase the production of ATP is addressed in Fig. 7. The increase in the rate of ATP synthesis (V_{ATPase}) with increasing Ca^{2+} is higher under push (+18.1%) rather than pull (+5.2%) conditions, although the V_{ATPase} is larger over the whole range of Ca^{2+} in the pull condition. In the region of high Ca^{2+}, the negative correlation between $\Delta\Psi_m$ and Ca^{2+} in the push condition (Fig. 7 *B*) results in a negative correlation between V_{ATPase} and Ca^{2+} (Fig. 7 *A*).

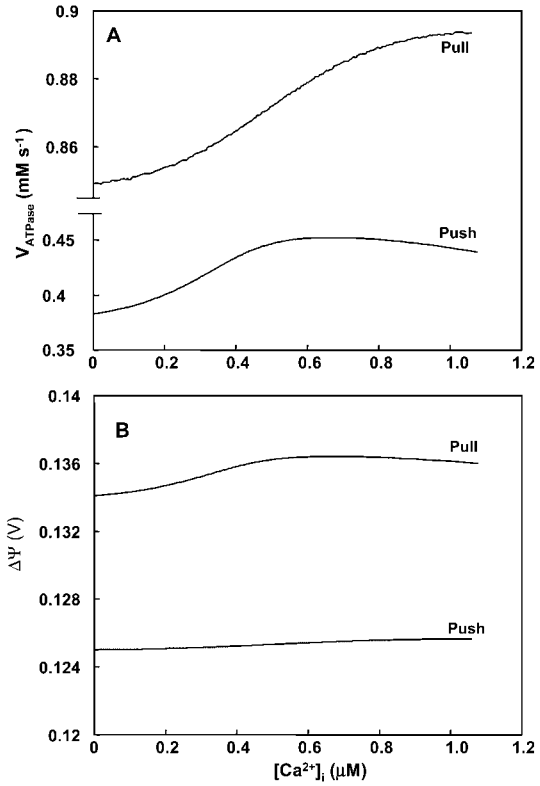

FIGURE 7 F_1F_0 ATP synthase activity and membrane potential as a function of $[Ca^{2+}]_i$. The different curves represent the rate of the mitochondrial ATP synthase, V_{ATPase} (*A*) and $\Delta\Psi_m$ (*B*) at steady state after an increase in $[Ca^{2+}]_i$, as shown in Fig. 5 with the same set of parameters described in its legend (*push* and *pull*).

The net difference between the stimulatory effect of Ca^{2+} on TCA cycle dehydrogenases and the dissipative effect of Ca^{2+} on $\Delta\Psi_m$ (Fig. 7 *B*) in turn determines the extent of stimulation or inhibition of ATP synthesis. Maximal stimulation occurs in the $\Delta\Psi_m$ range of maximal responsiveness, i.e., near the midpoint of the V_{ATPase} versus $\Delta\Psi_m$ curve (see Appendix Fig. A6, *B*). If $\Delta\Psi_m$ is too high or too low, the increase in ATP synthesis rate is negligible, even if respiration is stimulated strongly. The same reasoning explains why, in a condition of pull V_{ATPase} is stimulated marginally (+5.2% from 24 nM to 1.07 μM $[Ca^{2+}]_i$).

Metabolic control analysis of mitochondrial energetics

A control analysis of respiration has also been undertaken to further understand the control of mitochondrial respiration prevailing under the conditions analyzed above (Figs. 5–7). Control analysis is performed around the steady states given by $[Ca^{2+}]_i$ 0.1 and 0.5 μM (Fig. 5). The respiratory flux control coefficients shown in Table 2 are calculated by varying the V_{max} values of the different processes (see Methods).

Under push conditions, the main rate-controlling steps of respiration are the Ca^{2+}-sensitive dehydrogenases (KGDH and IDH) of the TCA cycle (Table 2). KGDH and IDH controlled 70% and 23%, respectively, of the respiratory flux when $[Ca^{2+}]_i$ stimulates the rates of respiration (Fig. 6 *A*), the F_1F_0-ATP synthase (Fig. 7 *A*) and the TCA cycle.

A large control by the respiratory chain and the ANT on the respiratory flux is obtained under pull conditions (Table 2). The latter situation corresponds closely to that described by Borutaite et al. (1995) regarding the control of respiration in heart mitochondria. Under these conditions, the processes downstream of NADH are flux-controlling (Table 2), but the ATP synthase is less stimulated by $[Ca^{2+}]_i$ (5.2%) when compared to the 18% increase registered under push conditions (Table 2). Thus, we conclude that $[Ca^{2+}]_i$ is better able to stimulate the rate of mitochondrial ATP synthesis when the TCA cycle exerts a significant control on respiration.

After a closer inspection of the initial reaction rate response of IDH and KGDH with respect to their substrates, only KGDH activity exhibits substantial elasticity to Ca^{2+} concentration within the stimulation range, in agreement with reported data (see Appendix Figs. A2 and A3; also see McCormack et al., 1990). This result explains why KGDH must exert a significant control on metabolism for respiratory flux to be stimulated by $[Ca^{2+}]_m$ (Figs. 5, and 6 *A*).

Time-dependent behavior of mitochondrial energetics during workload changes

The ability of the model to simulate time-dependent behavior was assessed by attempting to reproduce experimental data concerning mitochondrial NADH and Ca^{2+} dynamics obtained in heart trabeculae when challenged by changes in pacing frequency (Brandes and Bers, 1997, 2002). In these experiments, mitochondrial and cytoplasmic Ca^{2+} and NADH signals from rat heart trabeculae are simultaneously recorded during changes in the frequency of the electrical stimulation (Brandes and Bers, 2002). Increasing the pacing frequency from 0.25 Hz to 2 Hz results in the NADH concentration exhibiting an undershoot followed by a recovery phase to a new steady level (Fig. 8 *A*), whereas a decrease in the pacing frequency leads to an overshoot in NADH and slow relaxation of the signal back to the original baseline level.

An identical increase in pacing frequency in the mitochondrial model reveals a time course of $[Ca^{2+}]_m$ accumulation similar to the experimental results (Fig. 8 *C*), with $[Ca^{2+}]_m$ rising monotonically as the mitochondria function as an integrator of the pulsatile cytoplasmic Ca^{2+} transients, consistent with the previous results of Miyata et al. (1991).

Varying only the $[Ca^{2+}]_i$ transient driving function without changing ADP in the simulations results in a monotonic rise in NADH during an increase in pacing frequency

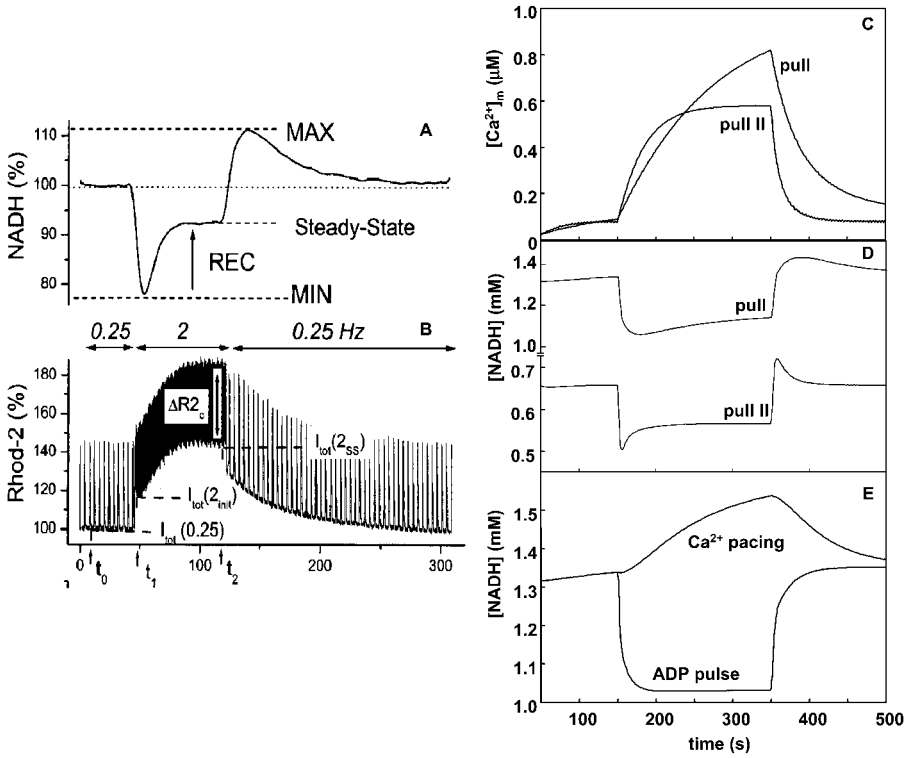

FIGURE 8 Time-dependent behavior of Ca^{2+} and NADH after changes in workload. (*A*, *B*) Experimental data showing the responses of NADH (*A*) and mitochondrial Ca^{2+} (*B*) to an increase in stimulation frequency from 0.25 to 2 Hz in a rat cardiac trabeculae (Reproduced from Brandes and Bers (2002) by copyright permission of the Biophysical Society). (*C*) Model response of mitochondrial Ca^{2+} to the pacing protocol described in Model Building and Numerical Methods, applied at low frequency (0.25 Hz) for 100 s, and then a high frequency (2 Hz) for 200 s, followed by a return to the low frequency. (*D*) Time course of NADH levels during changes in pacing frequency, simulated by increasing the Ca^{2+} pulse frequency combined with an increase in ADP_i. The "pull" parametric condition is similar to that defined in the legend of Fig. 5 except for $\rho^{RES} = 0.0006$, $\rho^{F1} = 1.787$ mM, and $V_{max}^{NaCa} = 0.05$ mM s^{-1}; "pull II" is similar to "pull" except $\rho^{RES} = 0.00072$ mM and $V_{max}^{NaCa} = 0.2$ mM s^{-1}. (*E*) The effects of a change in Ca^{2+} pulse frequency or ADP_i applied separately.

(0.25 Hz–2 Hz) and a monotonic decline upon decreasing frequency (Fig. 8 *E*).

A pulse of ADP (50–150 μM) in the absence of an increase in $[Ca^{2+}]_i$ pacing frequency results in a rapid decrease in NADH due to stimulation of the respiratory chain (pull condition) and recovery upon returning to the basal level (Fig. 8 *E*).

When the change in Ca^{2+} transient frequency and the increase in ADP are combined, model NADH concentration transients closely resemble the experimental data (Fig. 8 *D*). The rate of recovery of NADH can be accelerated by a small (20%) increase in respiration and a fourfold increase in V_{max}^{NaCa}. (Fig. 8 *D*; pull II). Fitting the curve of NADH recovery with a single exponential function renders $t_{1/2}$ values of 112 and 20 s for the conditions of pull and pull II, respectively. Mitochondrial Ca^{2+} relaxes with similar kinetics as NADH after the onset of high pacing frequency ($t_{1/2} = 127$ and 33 s for pull and pull II, respectively), resembling more closely the relaxations observed by Brandes and Bers (2002).

DISCUSSION

General

The main contribution of this modeling study is to link the TCA cycle, OxPhos, and mitochondrial Ca^{2+} dynamics through a mathematical model able to describe mitochondrial energetics based on well-known bioenergetic principles, i.e., the dependence of respiration on the redox potential and $\Delta\mu_H$, and the F_1F_0-ATPase on the phosphorylation potential and $\Delta\Psi_m$. The model is used to explore the interaction between mitochondrial energy metabolism and important extramitochondrial signals such as Ca^{2+} and substrate delivery. Several features distinguish this model from those presented previously: 1), the model integrates the kinetics of the TCA cycle with oxidative phosphorylation and Ca^{2+} handling (Fig. 1), 2), both thermodynamics and kinetics of the reactions are taken into account, permitting dynamic studies of enzyme kinetics and key metabolic intermediates as well as redox potential and $\Delta\Psi_m$ as the steady state is approached, and 3), the model incorporates the explicit dependence of the TCA cycle dehydrogenases on Ca^{2+}, allowing examination of the influence of Ca^{2+} on mitochondrial metabolism as a whole.

Metabolic control of oxidative phosphorylation

The integrative framework provided by the model makes it possible to analyze points of control of mitochondrial respiration by investigating how mitochondrial ATP production is matched to an increase in cardiac workload through increases of cytoplasmic Ca^{2+}.

Stimulation of respiration by ADP after changes in cellular ATP utilization has been proposed as one of the mechanisms by which mitochondrial ATP production meets the cellular ATP demand (respiratory control; see also Chance and Williams, 1956; Harris and Das, 1991). A shift from state 4 (respiration is low, $\Delta\mu_H$ is high, no ATP synthesis) to state 3

(respiration is high, $\Delta\mu_H$ is lowered by maximal ATP synthesis) is known to be accompanied by control redistribution in isolated mitochondria (Groen et al., 1982; Brown et al., 1990; Murphy, 2001). In cells, mitochondria are most often intermediate between states 3 and 4 (Ainscow and Brand, 1999; Murphy, 2001). The model reproduces the expected relationships between $\Delta\Psi_m$, V_{O_2}, and F_1F_0ATPase rate after shifts between states 3 and 4 when experiments simulating inhibition of the respiratory chain or the adenine nucleotide translocator are performed (Figs. 3, 4).

Control redistribution also occurs during impairment of mitochondrial function after ischemic injury. Mitochondria isolated from ischemic hearts show a decrease in respiratory capacity and a decrease in phosphorylation potential when respiring in the presence of succinate. These effects are more pronounced the longer the ischemic period, e.g., from 30 to 45 min (Borutaite et al., 1995). Such an inhibition of the respiratory chain, simulated here by reducing the concentration of electron carriers, results in a decreased respiration rate and a concomitant decrease in membrane potential (Fig. 4), consistent with experimental results (Fig. 4 *C*; see also Borutaite et al., 1995).

The model also reveals a steep dropoff of oxygen consumption as the concentration of electron carriers (ρ^{res}) reached a critical low level (Fig. 4 *A*). This type of threshold for disruption of mitochondrial function with respect to respiratory complex inhibition has been described previously (Murphy, 2001) and studied in vitro by titrating complex activity with irreversible inhibitors (Davey and Clark, 1996; Taylor et al., 1994; Rossignol et al., 1999). Maintenance of oxidative phosphorylation despite inhibition of a substantial fraction of the respiratory complexes may be explained by their high elasticities with respect to their substrates (Rossignol et al., 1999; Murphy, 2001). For example, partial inhibition of complex III will increase the ubiquinol/ubiquinone ratio, which would then increase the activity of uninhibited complexes. Thus, oxidative phosphorylation may be buffered against loss of respiratory chain components depending on the extent of inhibition of an individual complex required to decrease overall flux (Taylor et al., 1994). In our simulations, the threshold for collapse of respiration also depends on the inward flux of protons across the mitochondrial inner membrane (Fig. 4 *A*): when proton uptake is faster, the threshold ρ^{res} is shifted to a lower concentration range so that a greater fraction of carriers needs to be inhibited to affect respiration. It is important to note that ATP production would decrease before the decline in V_{O_2}, as a result of the drop in $\Delta\Psi_m$ at high proton uptake rates (Fig. 4 *B*).

Control by availability of substrate to the TCA cycle, AcCoA, may be relevant in the case of reperfusion of the heart after ischemia, inasmuch as TCA cycle flux is maintained or enhanced after brief ischemia (Weiss et al., 1993). The overall simulated flux through the TCA cycle in the range 0.05–0.1 mM s^{-1} (10–20 μmol *g* dry wt^{-1} min^{-1}), closely reproduces the global flux in whole hearts as reported in Jeffrey et al. (1999) and Williamson et al. (1976). Our results show that AcCoA levels exert control on respiratory flux, in parallel with NADH production, until saturation is reached (Fig. 2 *A*). As reported by Territo et al. (2001), substrate addition to isolated Ca^{2+}-depleted mitochondria increases the respiration rate by ~3.5-fold, $\Delta\Psi_m$ by ~30 mV (Fig. 2 *C*), and NADH by 7.7-fold. Similar trends are exhibited by V_{O_2}, NADH, and $\Delta\Psi_m$ in the simulations shown in Fig. 2.

Effects of Ca^{2+} on mitochondrial energetics

The inotropic mechanisms activated in response to an increase in cardiac workload (e.g., an increase in heart rate and/or Ca^{2+} release) also increase the time-averaged Ca^{2+} in the cytoplasm: this has been proposed as a control factor for increasing mitochondrial ATP production (Harris and Das, 1991; Territo et al., 2000, 2001).

An increase in $[Ca^{2+}]_i$ has two opposite effects on mitochondria: a stimulatory effect on the activity of the TCA cycle dehydrogenases as a consequence of higher $[Ca^{2+}]_m$ (Figs. 5 and 6), and a dissipative effect on the inner mitochondrial membrane potential due to the influx of the divalent cation. The balance between these two effects is reflected by $\Delta\Psi_m$. In isolated mitochondria, Ca^{2+} stimulation can increase NADH (McCormack et al., 1990; Hansford and Zorov, 1998; Territo et al., 2000), but the magnitude of this increase will also depend on any downstream effects on NADH oxidation. Flux through the electron transport chain will be accelerated by dissipation of $\Delta\mu_H$, which could be caused by an increase in F_1F_0-ATPase velocity (due to increased ADP availability or direct stimulation of the ATPase (Territo et al., 2001)), or by non-ATPase-mediated energy dissipating pathways such as Ca^{2+} influx (relevant to the present model simulations) or enhanced proton leak. Non-ATPase energy dissipation will increase V_{O_2} without necessarily increasing ATP production; however, our model simulates both an increase in V_{ATPase} and an increase in V_{O_2} as a function of $[Ca^{2+}]_i$ (Figs. 6 *A* and 7 *A*), demonstrating that TCA cycle stimulation is adequate to bolster NADH levels and $\Delta\Psi_m$ (Figs. 6 *B* and 7 *B*). The increase in the rate of ATP production by the mitochondria after an increase in $[Ca^{2+}]_i$ from 20 to 660 nM is ~18%, a moderate change relative to the increase in V_{O_2} (usually more than 20% increase; Figs. 6 *A* and 7 *A*).

In the framework of the present model, the control of the respiratory flux at the mitochondrial level may be exerted by processes upstream and downstream of NADH (Table 2). Mitochondrial energetics is in a condition of push when respiration is controlled mainly by processes upstream of NADH, i.e., the TCA cycle. In this regard, a significant stimulation of ATP synthesis by Ca^{2+} can be achieved when respiration is controlled at the level of the Ca^{2+}-sensitive dehydrogenases (Table 2: push). A drawback of the push

condition is that the NADH levels produced by the model are lower than those determined experimentally (e.g., Brandes and Bers, 1997). Under pull conditions, downstream processes such as ANT or respiration itself, are the main rate-controlling steps of respiration (Table 2: pull).

Experimental data obtained for isolated rat liver cells show that control of respiration and oxidative phosphorylation is primarily downstream of NADH (Brown et al., 1990). Accordingly, rat liver mitochondria would be predominantly in the pull condition, inasmuch as 49% of the control is exerted by the processes of ATP synthesis, transport and consumption, 22% by proton cycling not coupled to ATP synthesis, and only 29% by respiration and upstream processes. Brown et al. (1990) estimated that 15–30% of the control over respiration would be exerted by processes involved in NADH generation. In our simulations, under pull conditions, the stimulation of oxidative phosphorylation by increasing cytosolic Ca^{2+} concentration is diminished (Figs. 6 and 7). Thus, the further incorporation of Ca^{2+}-activated cytosolic ATPases, such as those involved in Ca^{2+} handling and muscle contraction, may be required in the future, to better couple the acceleration of V_{O_2} with the V_{ATPase} and increase the contribution of downstream pull on the system. In this regard, Territo et al. (2000) have reported that addition of Ca^{2+} to isolated mitochondria stimulated O_2 consumption as well as NADH levels. Determining ATP contents in mitochondrial preparations subjected to increasing Ca^{2+} concentrations, they inferred a stimulation of the ATP synthase activity. To account for these findings, they concluded that the F_1F_0-ATPase must be directly activated by Ca^{2+} (Territo et al., 2000, 2001). Nevertheless, it is notable that we can simulate an increase in ATPase activity upon increasing $[Ca^{2+}]_i$ without invoking other mechanisms of activation apart from the known biochemical and biophysical principles ruling mitochondrial bioenergetics. Stimulation depends only on the driving forces involved: the phosphorylation potential and the proton motive force. Obviously, inasmuch as the model simulations can reproduce different control properties of the system, they cannot provide an unequivocal quantitative answer to the relative contributions of upstream and downstream control mechanisms in living tissues. Therefore, we do not presume to strongly favor one control point over another for all cases; however, the model provides important feasibility arguments to be tested in future experimental studies.

An additional limitation of model interpretation lies in the absence of spatial organization of the mitochondria and cellular structures. For example, intracellular compartmentation of the adenine nucleotide pool has been proposed as an alternative explanation to Ca^{2+} activation in the context of matching of energy production and demand. It has been argued that cardiac contractile failure during ischemia or hypoxia still happens despite high ATP contents (70–80% of normal ATP content), leading to the hypothesis that a localized metabolic compartment may be present in which larger changes in phosphorylation potential occur. There is evidence for metabolic compartmentation (reviewed in Saks et al., 1998) and such metabolite channeling may be due to the close proximity of energy-consuming and energy-producing sites or to the actions of the creatine phosphate shuttle (Saks et al., 2001).

Similarly, the close apposition of sarcoplasmic reticular Ca^{2+} release sites and mitochondria may create a local Ca^{2+} microdomain, in which Ca^{2+} concentrations might be much higher than the bulk phase. Experimental evidence for fast uptake of mitochondrial Ca^{2+} has been reported (Rizzuto et al., 1998; Duchen et al., 1998). Our simulation results of the dynamics of Ca^{2+} uptake in response to pulses of $[Ca^{2+}]_i$ indicate that mitochondrial Ca^{2+} must essentially act as an integrator of cytosolic Ca^{2+} to reproduce intact muscle behavior (Fig. 8). This is another area in which spatial considerations and alternative Ca^{2+} uptake pathways may be incorporated in the future.

Time-dependent behavior of mitochondrial energetics

The ability of the model to simulate time-dependent behavior is indeed the most rigorous test of its validity, and emphasizes the utility of a model based on realistic kinetic properties of its components. We have been able to closely reproduce the NADH evolution in rat heart trabeculae when challenged by increases in workload through the pacing frequency of electrical stimulation (Brandes and Bers, 2002). The temporal profile of NADH evolution found experimentally can be simulated (compare Fig. 8, *A* and *D*). To reproduce the observed NADH transients, we have to incorporate an increase in ADP to represent increased cellular ATPase activity together with the increase in the pacing frequency of $[Ca^{2+}]_i$. Thus, the model results suggest a co-participation of Ca^{2+} and ADP to explain mitochondrial NADH dynamics during an increase in workload. Additionally, we conclude that the under- and over-shoots of mitochondrial NADH during changes in pacing frequency are due to the rapid effects of ADP on respiration followed by the slower adaptation of the Ca^{2+}-sensitive dehydrogenase activities. These results point out the involvement of respiratory control and activation of dehydrogenases by Ca^{2+} in the coupling between energy supply and demand in cardiac myocytes challenged by changes in workload.

Previous models of energetics

Previously, the most comprehensive metabolic models of cardiac metabolism were reported by Kohn and co-workers, to describe the energetics of the rat heart consuming different carbon substrates (Kohn and Garfinkel, 1979; 1983). Glycolysis, fatty acid oxidation, the TCA cycle, a lumped

system representing mitochondrial respiration and oxidative phosphorylation, and chelation equilibria for nucleotides and organic acids were included in this model. However, these models were essentially based on mass action laws, with the assumption that most of the metabolic steps were reversible.

Other TCA cycle models were specifically developed for interpreting the data from NMR studies of whole hearts (Weiss et al., 1992, 1993; Yu et al., 1997; Tran-Dinh et al., 1996; Jeffrey et al., 1999). In such cases, the model equations were designed to fit the evolution of the ^{13}C enrichment profiles of various TCA cycle intermediates, following the approach of Chance et al. (1983). The tracer equations used in these models do not address any explicit kinetic mechanism of each enzyme participating in the TCA cycle.

Other models of the TCA cycle have been developed for the amoeba *Dictyostelium discoideum* based on data about the temporal evolution of tracers (Wright et al., 1992; Shiraishi and Savageau, 1992). Wright and collaborators (1992) based their model on Michaelis-Menten kinetics taking into account the kinetic constants for substrates, products and some effectors obtained from the in vitro characterization of enzyme kinetics. Shiraishi and Savageau (1992), in turn, developed a model based on the power law formalism. Both models appropriately describe the behavior of the system for a certain range of parametric conditions. However, none of those models account for the effect of Ca^{2+}, which is of central importance to cardiac mitochondrial energetics.

A model of pancreatic β-cell mitochondrial metabolism by Magnus and Keizer (1997), which incorporates Ca^{2+} handling by mitochondria, involves three ordinary differential equations describing $\Delta\Psi_m$, Ca^{2+}, and ADP concentrations as a function of time. This model takes into account the most important transport processes of the inner mitochondrial membrane, i.e., redox-driven proton pumps, the F_1F_0-ATPase, proton leak, the adenine nucleotide transporter, the Ca^{2+} uniporter, and the mitochondrial Na^+/Ca^{2+} exchanger. Important limitations of this model are that it does not include stimulation of TCA cycle dehydrogenases by Ca^{2+} and that NADH is a fixed parameter (Magnus, 1995; Magnus and Keizer, 1997) instead of a variable (as in the present model). Nevertheless, in agreement with experimental data, the model behavior was able to reproduce the dependence of the rate of Ca^{2+} uptake by the uniporter on cytosolic Ca^{2+} concentration and predicts a sharp threshold for uptake at cytosolic Ca^{2+} concentrations of $\sim$0.4–0.5 μM (Magnus and Keizer, 1997).

An oxidative phosphorylation mathematical model has been developed by Korzeniewski (1996, 1998) and applied to the analysis of how the rate of ATP production by respiration is adjusted to meet energy demand during muscle contraction (Korzeniewski, 1998). As in previous cases, this model does not account for the coupling of OxPhos to the TCA cycle and thus no explicit dependence on Ca^{2+} by TCA cycle dehydrogenases was taken into account.

CONCLUSION

In summary, the integrated thermokinetic model constructed here reproduces the expected relationships among $\Delta\Psi_m$, V_{O_2}, NADH, and mitochondrial matrix Ca^{2+} accumulation under various conditions including simulated inhibition of respiratory chain complexes and/or adenine nucleotide translocase.

Based solely on simple bioenergetic principles, it is demonstrated that Ca^{2+} activation of the TCA cycle, NADH production, mitochondrial respiration, and ATP synthesis is possible when respiratory flux is mainly controlled by the Ca^{2+}-sensitive KGDH. During changes in workload, under pull conditions, both respiratory control and stimulation by Ca^{2+} appear to be required to reproduce the temporal evolution of NADH in heart trabeculae. Under other parametric conditions, supplemental control mechanisms for oxidative phosphorylation may be necessary to account for experimental data. Increased ATP production by Ca^{2+} can only be achieved when the extent of stimulation of NADH production exceeds the energy-dissipating effect of Ca^{2+} influx on $\Delta\Psi_m$.

This comprehensive model of cardiac mitochondrial metabolism will permit testing of bioenergetic control hypotheses, provide a basis for further refinement of individual steps of oxidative phosphorylation and mitochondrial Ca^{2+} handling, and allow for future incorporation of other biochemical pathways.

APPENDIX

The model has three main components: mitochondrial matrix processes, oxidative phosphorylation, and Ca^{2+} dynamics.

The tricarboxylic acid (TCA) cycle

In the mitochondrial matrix, we have considered the dynamics of the TCA cycle that represents the end stage for carbon-chain metabolic substrates in the cell.

The TCA cycle in our model may be split into two pathways: the tricarboxylate (from oxalacetate, OAA, to α-ketoglutarate, αKG, via citrate, CIT) and the dicarboxylate (from αKG to OAA via succinate, Suc; see also Fig. 1) (Jafri et al., 2001). In the tricarboxylate pathway AcCoA and OAA react to produce αKG, NADH, and CO_2. In turn, αKG serves as a substrate of the dicarboxylate pathway producing OAA that will resupply the first pathway. Alternatively, a shunt may directly lead from OAA into αKG through the aspartate amino transferase (AAT)-catalyzed reaction (Fig. 1).

The model includes detailed kinetics of the key regulatory enzymes of the TCA cycle with respect to their effectors such as Ca^{2+}, Mg^{2+}, ADP, NADH, and NAD^+, as well as their carbon substrates (Dudycha, 2000; Jafri et al., 2001).

Unlike succinate dehydrogenase (SDH), aconitase, succinyl CoA lyase, and fumarate hydratase are considered to operate under near equilibrium conditions.

Citrate synthase (CS)

The first enzyme of the cycle is CS that catalyzes the condensation of OAA and AcCoA to give CIT. The kinetic rate law (Eq. 13) we used was modified

from that derived by Dudycha (2000) based on data by Shepherd and Garland (1969):

$$V_{CS} = \frac{k_{cat}^{CS} E_T^{CS}}{1 + \frac{K_M^{AcCoA}}{[AcCoA]} + \frac{K_M^{OAA}}{[OAA]} + \frac{K_M^{AcCoA}}{[AcCoA]} \frac{K_M^{OAA}}{[OAA]}}. \quad (13)$$

Since the TCA cycle and the AAT shunt are closed from the point of view of carbon intermediates, a conservation equation relating all TCA metabolites is included in the model. Thus, the level of CIT is the result of the balance of all other intermediates in the cycle as follows:

$$[CIT] = C_{Kint} - [ISOC] - [\alpha KG] - [SCoA] - [Suc] - [FUM] - [MAL] - [OAA] \quad (14)$$

with C_{Kint} as the total concentration of TCA cycle intermediates.

CS is studied as a function of the concentrations of its substrates, OAA and AcCoA, and displays saturating activity with respect to both (Fig. A1, *A* and *B*). Saturation is achieved at low concentrations of OAA. Low levels of this intermediate have been estimated from in vivo measurements and theory (Jeffrey et al., 1999). This result supports the operation of CS at high rate at low concentrations of its substrate OAA.

Aconitase (ACO)

ACO is considered to be operating near equilibrium as reported data in the literature suggest (Jeffrey et al., 1999) (Eq. 15).

$$V_{ACO} = k_f^{ACO}\left([CIT] - \frac{[ISOC]}{K_E^{ACO}}\right). \quad (15)$$

The kinetic expression of Eq. 15 is based on the law of mass action and assumes that the enzyme operates reversibly near equilibrium, characterized by an equilibrium constant, K_E^{ACO}.

Isocitrate dehydrogenase (IDH)

IDH is one of the matrix dehydrogenases regulated by calcium. Additionally, IDH is activated by ADP and inhibited by its product, NADH (Fig. 1). Moreover, it shows a sigmoidal dependence on isocitrate, ISOC (Rutter and Denton, 1988).

$$V_{IDH} = \frac{k_{cat}^{IDH} E_T^{IDH}}{\left(1 + \frac{[H^+]}{k_{h,1}} + \frac{k_{h,2}}{[H^+]}\right) + \frac{\left(\frac{K_M^{ISOC}}{[ISOC]}\right)^{ni}}{\left(1 + \frac{[ADP]_m}{K_{ADP}^a}\right)\left(1 + \frac{[Ca^{2+}]_m}{K_{Ca}^a}\right)} + \left(\frac{K_M^{NAD}}{[NAD]}\right)\left(1 + \frac{[NADH]}{K_{i,NADH}}\right) + \frac{\left(\frac{K_M^{ISOC}}{[ISOC]}\right)^{ni}\left(\frac{K_M^{NAD}}{[NAD]}\right)\left(1 + \frac{[NADH]}{K_{i,NADH}}\right)}{\left(1 + \frac{[ADP]_m}{K_{ADP}^a}\right)\left(1 + \frac{[Ca^{2+}]_m}{K_{Ca}^a}\right)}} \quad (16)$$

IDH activity exhibits a modest response to Ca^{2+} in the concentration range described in vivo (Fig. A2, *A*). The rate of IDH is more sensitive to Ca^{2+} concentrations near saturation of the activity with respect to the substrate ISOC (Fig. A2, *A*). The quasi-exponential dependence of IDH with respect to NAD^+ is due primarily to the strong inhibitory effect exerted by NADH on the enzymatic activity. Inasmuch as NAD^+ and NADH are constrained by a conservation relationship, an increase in NAD^+ implies a decrease in NADH and strong activation of enzyme activity as postulated (Fig. A2, *B*).

Alpha-ketoglutarate dehydrogenase (KGDH)

KGDH is another Ca^{2+}-sensitive dehydrogenase participating in the TCA cycle. The rate expression for this enzyme was derived from Dudycha (2000) fitting data from Panov and Scarpa (1996). We have modified several of the parameters used by Dudycha (2000) to reproduce the experimental data from Rutter and Denton (1988).

$$V_{KGDH} = \frac{k_{cat}^{KGDH} E_T^{KGDH}}{1 + \frac{\left(\frac{K_M^{\alpha KG}}{[\alpha KG]}\right)^{n_{aKG}}}{\left(1 + \frac{[Mg^{2+}]}{K_D^{Mg^{2+}}}\right)\left(1 + \frac{[Ca^{2+}]_m}{K_D^{Ca^{2+}}}\right)} + \frac{\left(\frac{K_M^{NAD}}{[NAD]}\right)}{\left(1 + \frac{[Mg^{2+}]}{K_D^{Mg^{2+}}}\right)\left(1 + \frac{[Ca^{2+}]_m}{K_D^{Ca^{2+}}}\right)}} \quad (17)$$

Unlike IDH, KGDH shows a marked dependence on Ca^{2+} concentration in the physiological range (Fig. A3, *A*). This highlights one of the main conditions for the model to exhibit a maximal response to Ca^{2+} concentrations, KGDH needs to be the main rate-controlling step of respiratory flux. Also unlike IDH, the kinetics of KGDH are saturable with respect to NAD^+, with the maximal activation by NAD^+ depending on αKG levels (Fig. A3, *B*).

Succinyl CoA lyase (SL)

SL catalyzes the conversion of SCoA into Suc, involving the direct phosphorylation of GDP (Kadrmas et al., 1991). In our model we have assumed rapid equilibration of the GTP and ATP pools via a matrix nucleoside diphosphate kinase (Colomb et al., 1972). Thus, the rate equation for SL is ruled by the following expression, including mitochondrial ADP and ATP levels:

$$V_{SL} = k_f^{SL}\left([SCoA]\,[ADP]_m - \frac{[Suc]\,[ATP]_m[CoA]}{K_E^{SL}}\right). \quad (18)$$

Succinate dehydrogenase (SDH)

SDH catalyzes the reduction of ubiquinone by succinate, coupled with the formation of fumarate and ubiquinol. It is the only enzyme of the TCA cycle which is bound to the inner membrane of mitochondria, directly linking the TCA cycle to the electron transport chain at complex II. The kinetic properties of SDH have been extensively studied (reviewed by Singer et al., 1973, and Hatefi and Stiggall, 1976). Its reaction rate is subject to inhibition by its product, FUM, and by OAA (Fig. 1; see also Singer et al., 1973; Hatefi

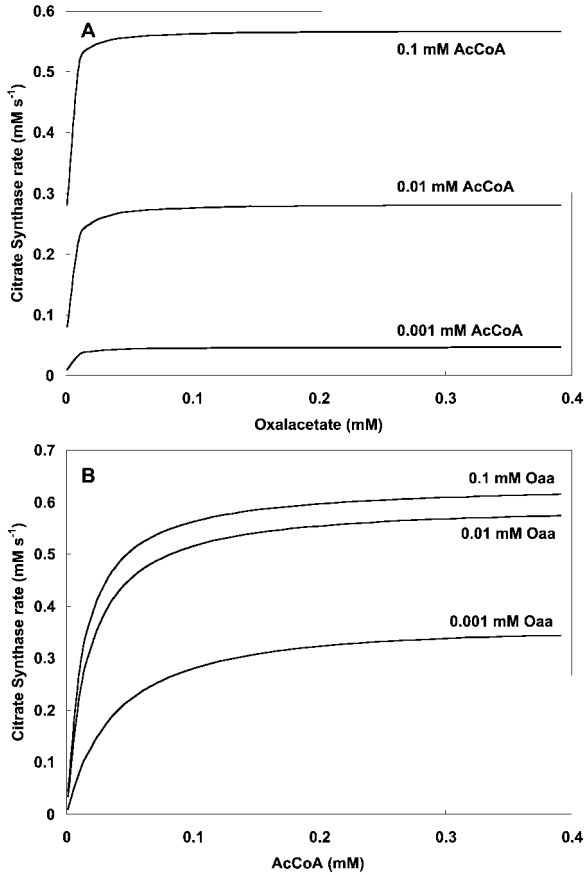

FIGURE A1 Dependence of citrate synthase activity on oxalacetate and AcCoA. (*A*) The rate of CS is plotted against oxaloacetate concentration with $k_{cat}^{CS} = 1.6\ s^{-1}$ at the specified AcCoA concentrations and parameter values according to Table 3 (see Eq. 13). (*B*) The same parameter set is used to study CS activity as a function of AcCoA at different oxalacetate concentrations.

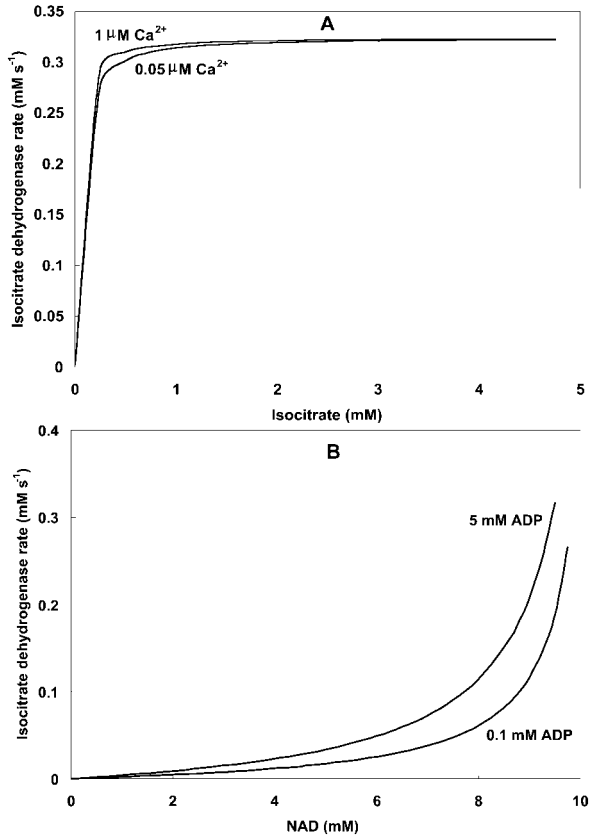

FIGURE A2 Isocitrate dehydrogenase activity as a function of substrate and Ca^{2+} concentrations. (*A*) The rate of IDH is studied as a function of isocitrate and Ca^{2+} concentrations in the physiological range (see Eq. 16). The analysis was performed with the following parameter values: $[NAD^+] = 9.5$ mM; $[ADP]_m = 2.0$ mM; $E_T^{IDH} = 0.109$ mM; $k_{cat}^{IDH} = 16.3\ s^{-1}$ and those described in Table 3. (*B*) The IDH dependence on NAD^+ concentration is analyzed at different ADP concentrations with [ISOC] = 0.5 mM, and $[Ca^{2+}] = 0.5\ \mu$M. Otherwise the parameters used are as in *A*.

and Stiggall, 1976). The rate expression is described by the following equation:

$$V_{SDH} = \frac{k_{cat}^{SDH} E_T^{SDH}}{1 + \left(\frac{K_M^{Suc}}{[Suc]}\right)\left(1 + \frac{[OAA]}{K_{i,sdh}^{OAA}}\right)\left(1 + \frac{[FUM]}{K_i^{FUM}}\right)}. \quad (19)$$

parameters of the equation have been adjusted based on the data reported by Elduque and co-workers (1983).

$$V_{MDH} = \frac{k_{cat}^{MDH} E_T^{MDH} f_{h,a} f_{h,i}}{1 + \frac{K_M^{MAL}}{[MAL]}\left(1 + \frac{[OAA]}{K_i^{OAA}}\right) + \frac{K_M^{NAD}}{[NAD]} + \frac{K_M^{MAL}}{[MAL]}\left(1 + \frac{[OAA]}{K_i^{OAA}}\right)\frac{K_M^{NAD}}{[NAD]}} \quad (21)$$

Fumarate hydratase (FH)

FH is considered to operate near equilibrium and the kinetic parameters are taken from Dudycha (2000) based on data from Teipel and Hill (1971). Its rate expression is as follows:

$$V_{FH} = k_f^{FH}\left([FUM] - \frac{[MAL]}{K_E^{FH}}\right). \quad (20)$$

Malate dehydrogenase (MDH)

MDH is another highly regulated TCA cycle enzymatic activity. MDH is inhibited by its product, OAA, and modulated by pH (Dudycha, 2000). The

with

$$f_{h,a} = \frac{1}{1 + \frac{[H^+]}{k_{h1}} + \frac{[H^+]^2}{k_{h1} k_{h2}}} + k_{offset} \quad (22)$$

and

$$f_{h,i} = \left(\frac{1}{1 + \frac{k_{h3}}{[H^+]} + \frac{k_{h3} k_{h4}}{[H^+]^2}}\right)^2. \quad (23)$$

Fig. A4 shows the MDH activity as a function of its substrate, malate (MAL), at different NAD^+ concentrations. MDH displays typical Michaelis-Menten kinetics that saturate at high substrate concentrations, which are at least two orders of magnitude higher than the actual MAL levels determined in myocytes (Albe et al., 1990).

Aspartate amino transferase (AAT)

AAT activity constitutes a shunt linking directly OAA to αKG. This activity is considered to be working close to equilibrium in the presence of a large excess of glutamate, GLU (Eq. 24).

$$V_{AAT} = k_f^{AAT}\left([OAA][GLU] - \frac{[\alpha KG][ASP]}{K_E^{AAT}}\right). \quad (24)$$

The aspartate (ASP) resulting from AAT activity is assumed to be consumed in a reaction that follows a mass action law with respect to its substrate ASP, as follows:

$$V_{C\_ASP} = k_{C\_ASP}\,[ASP]. \quad (25)$$

Differential Eqs. 3–11 are assembled from this group of processes in the model. The parameters of Eqs. 13–25 for this section of the model description are described in the module: *TCA cycle* in Table 3.

Oxidative phosphorylation

The respiration-driven proton pump

The main reaction steps described are the O_2 consumption flux, V_{O_2}, and its linked proton efflux, V_{He}. The rate of these two processes depends on $\Delta\mu_H$ and the redox potential as driving forces. Eqs. 26–28 describe the flow of electrons from NADH to O_2 and its associated proton flux from the matrix to the intermembrane space in mitochondria (Magnus and Keizer, 1997). In adapting the Altman-King-Hill-based model of the respiration-driven proton pump for heart mitochondria, we have considered the electron flow from NADH oxidation to be incompletely coupled to the outward flow of protons, V_{He} as in Magnus (1995) and Magnus and Keizer (1997).

$$V_{O_2} = 0.5\rho^{res}\frac{\left(r_a + r_{c1}\,e^{(6F\Delta\Psi_B/RT)}\right)e^{(A_{res}F/RT)} - r_a\,e^{(g6F\Delta\mu_H/RT)} + r_{c2}\,e^{(A_{res}F/RT)}\,e^{(g6F\Delta\mu_H/RT)}}{\left(1 + r_1\,e^{(FA_{res}/RT)}\right)e^{(6F\Delta\Psi_B/RT)} + \left(r_2 + r_3\,e^{(FA_{res}/RT)}\right)e^{(g6F\Delta\mu_H/RT)}} \quad (26)$$

$$V_{He} = 6\rho^{res}\frac{\left(r_a\,e^{(A_{res}F/RT)} - \left(r_a + r_b\right)e^{(g6F\Delta\mu_H/RT)}\right)}{\left(1 + r_1\,e^{(FA_{res}/RT)}\right)e^{(6F\Delta\Psi_B/RT)} + \left(r_2 + r_3\,e^{(FA_{res}/RT)}\right)e^{(g6F\Delta\mu_H/RT)}} \quad (27)$$

with

$$A_{res} = \frac{RT}{F}\ln\left(K_{res}\sqrt{\frac{[NADH]}{[NAD^+]}}\right). \quad (28)$$

Another very important modification of the previous model is that we have replaced the dependence of the respiratory flux on $\Delta\mu_H$ instead of just the electrical potential, $\Delta\Psi_m$. This is done so as not to ignore the transmembrane proton concentration gradient (ΔpH) component of the proton motive force (Eqs. 26, 27). Thus, we assume that most transitions between the six states in the proton pump model (Magnus, 1995; Magnus and Keizer, 1997) depend on both $\Delta\Psi_m$ and ΔpH through $\Delta\mu_H$.

In a modification of the original formulation, we also consider the complex II electrons input by succinate (Suc) through $FADH_2$ to the respiratory chain:

$$Suc \Leftrightarrow Fum + 2\,e^- + 2\,H^+ \qquad \varepsilon^0 = +0.031\ V$$

$$\frac{1}{2}O_2 + 2H^+ + 2\,e^- \Leftrightarrow H_2O \qquad \varepsilon^0 = 0.815\ V$$

rendering

$$\frac{1}{2}Suc + \frac{1}{4}O_2 \Leftrightarrow \frac{1}{2}Fum + \frac{1}{2}H_2O \quad \Delta\varepsilon^0 = +0.846\ V$$

$$K_{eq} = e^{\Delta\varepsilon^0 F/RT} = 5.765\ 10^{13}$$

K_{eq} in Eq. 29 reads as $K_{res(F)}$:

$$A_{res(F)} = \frac{RT}{F}\ln\left(K_{res(F)}\sqrt{\frac{[FADH_2]}{[FAD]}}\right). \quad (29)$$

The flux of protons driven by $FADH_2$ oxidation ($V_{He(F)}$) has the same form as Eq. 27 except for adjustment of the redox potential (Eq. 29) and the H^+ stoichiometry (four instead of six). A careful analysis reveals that the sensitivity of the overall O_2 consumption with complex II is very low, which leads us to consider $FADH_2$ as a parameter in our model.

Mitochondrial NAD^+ is assumed to be conserved according to the following relation:

$$[NAD^+] = C_{PN} - [NADH], \quad (30)$$

with C_{PN} as the total concentration of pyrimidine nucleotides.

Oxygen consumption rate (V_{O_2}) is studied as a function of NADH and $\Delta\Psi_m$ (Fig. A5). NADH exerts its influence on V_{O_2} through the redox potential A_{res} (Eqs. 26, 28), with the shape of the curve depending on $\Delta\Psi_m$ (Fig. A5, *A*); i.e., at high $\Delta\Psi_m$, the dependence of V_{O_2} on NADH becomes shallower, as it becomes more difficult to pump protons against a high $\Delta\mu_H$. The decrease in V_{O_2} at high $\Delta\Psi_m$ is evident in Fig. A5, *B*. The midpoint of this flux-force relation is shifted to the left by an increase in the ΔpH component of $\Delta\mu_H$ (Fig. A5, *B*). Around the midpoint, the relationship between V_{O_2} and $\Delta\Psi_m$ is almost linear, but outside this range the rate of respiration becomes independent of $\Delta\Psi_m$ (Fig. A5, *B*).

The F_1F_0-ATPase

The rate of the F_1F_0-ATPase from Magnus and Keizer (1997) was modified to account for reversibility (Eq. 31). A factor of 10^2 was introduced in the first term of Eq. 31 and the value of the sum of products of rate constants p_{c2} was increased with respect to the original value (Magnus and Keizer, 1997; see also Table 3, this article). These modifications together with the substitution of $\Delta\Psi_m$ by $\Delta\mu_H$ in Eqs. 31 and 32 allow reversibility of the H^+ pump when $\Delta\mu_H$ falls below a certain value or at very high phosphorylation potentials.

According to the concept of respiratory control (Chance and Williams, 1956), in state 3, mitochondrial function is governed by the availability of ADP and P_i. The chemiosmotic hypothesis dictates that $\Delta\Psi_m$ is lowered by a H^+ influx, which drives the production of ATP by the F_1F_0-ATPase. Escape from respiratory control results in higher O_2 consumption, electron transfer, and substrate oxidation that is not coupled to phosphorylation of ADP, and a decrease in the P:O ratio (Mitchell, 1969).

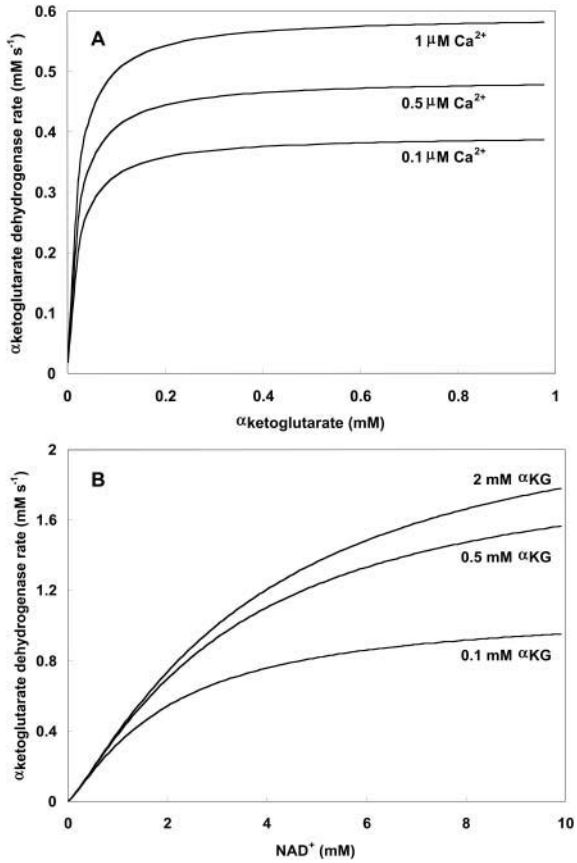

FIGURE A3 Alpha-ketoglutarate dehydrogenase dependence on α-ketoglutarate, NAD^+, and Ca^{2+}. (*A*) The set of parameters used in the analysis of the rate of KGDH (V_{KGDH}) as a function of its substrate is as indicated in Table 3 (see also Eq. 17) with the following modifications: $E_T^{KGDH} = 0.5$ mM; $k_{cat}^{KGDH} = 5.0\ s^{-1}$; $[NAD^+] = 1.0$ mM; and $[Mg^{2+}] = 0.4$ mM. (*B*) The analysis of the dependence of V_{KGDH} on NAD^+ concentration is performed with the following parameter values: $[Mg^{2+}] = 0.4$ mM, and $[Ca^{2+}] = 0.1$ μM. Otherwise the parameters used are as in *A*.

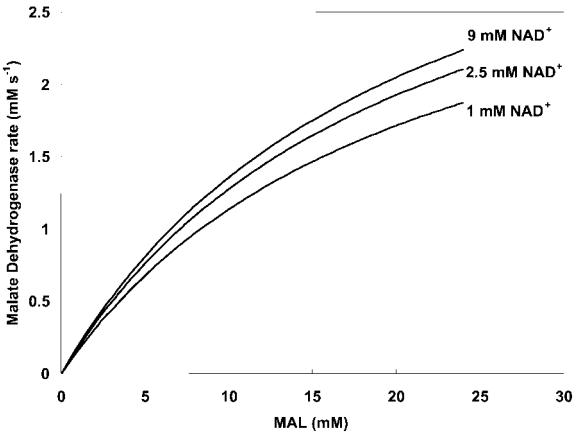

FIGURE A4 Malate dehydrogenase activity as a function of substrate concentration. The dependence of MDH rate on its substrate malate is studied with the following parameter values: $E_T^{MDH} = 0.154$ mM, $k_{cat}^{MDH} = 27.75\ s^{-1}$, and those shown in Table 3 (see also Eq. 21).

with C_m as the total sum of adenine nucleotides and $[ADP]_m$ as the mitochondrial ADP concentration.

The dependence of F_1F_0-ATPase rate on its substrate, ADP, is illustrated in Fig. A6, *A*. At low concentrations of ADP_m (state 4 respiration), the thermodynamics of the pump favors ATP hydrolysis (shown by convention as a negative velocity) depending on $\Delta\Psi_m$ (Eq. 2). An accumulation of ADP_m tends to shift mitochondrial energetics toward state 3, and net ATP synthesis (positive velocity). Thus, the relationship between F_1F_0-ATPase activity and $[ADP]_m$ depends on $\Delta\Psi_m$; at higher $\Delta\Psi_m$, less $[ADP]_m$ is required for the F_1F_0-ATPase to achieve its maximal rate and the forward (synthetic) mode is favored (Fig. A6, *A*). Inasmuch as $\Delta\mu_H$ is the actual driving force for ATP synthesis, the forward mode is enhanced at any given $\Delta\Psi_m$ as ΔpH increases (Fig. A6, *B*).

Adenine nucleotide translocator (ANT) and proton leak

To complete the description of the major membrane-OxPhos-associated processes, the exchange of adenine nucleotides across the mitochondrial membrane as well as a proton leak, are considered (Fig. 1).

$$V_{ATPase} = -\rho^{F1}\frac{(10^2 p_a + p_{c1}\, e^{(3F\Delta\Psi_B/RT)})\, e^{(A_{F1}F/RT)} - (p_a\, e^{(3F\Delta\mu_H/RT)} + p_{c2}\, e^{(A_{F1}F/RT)}\, e^{(3F\Delta\mu_H/RT)})}{(1 + p_1\, e^{(FA_{F1}/RT)})\, e^{(3F\Delta\Psi_B/RT)} + (p_2 + p_3\, e^{(FA_{F1}/RT)})\, e^{(3F\Delta\mu_H/RT)}} \tag{31}$$

$$V_{Hu} = -3\rho^{F1}\frac{10^2 p_a(1 + e^{(FA_{F1}/RT)}) - (p_a + p_b)\, e^{(3F\Delta\mu_H/RT)}}{(1 + p_1\, e^{(FA_{F1}/RT)})\, e^{(3F\Delta\Psi_B/RT)} + (p_2 + p_3\, e^{(FA_{F1}/RT)})\, e^{(3F\Delta\mu_H/RT)}} \tag{32}$$

with

$$A_{F1} = \frac{RT}{F}\ln\left(K_{F1}\frac{[ATP]_m}{[ADP]_m Pi}\right). \tag{33}$$

Mitochondrial ATP, $[ATP]_m$, is assumed to be conserved according to the following relation:

$$[ATP]_m = C_m - [ADP]_m, \tag{34}$$

The ANT is modeled according to a sequential mechanism of the carrier (Magnus and Keizer, 1997; Bohnensack, 1982). Oppositely oriented sites bind either ATP^{4-} or ADP^{3-}, and both sites must be filled before the protein isomerization causes a ligand exchange across the inner membrane. V_{ANT}, the flux of ANT-mediated exchange between cytosolic ADP (ADP_i) and matrix ATP (ATP_m) (Eq. 35) is considered to be electrogenic and dependent on the gradients of both ATP and ADP across the inner mitochondrial membrane as follows:

$$V_{ANT} = V_{maxANT}\frac{\left(1 - \dfrac{0.05\times[ATP]_i\times 0.45\times 0.8\times[ADP]_m}{0.45\times[ADP]_i\times 0.05\times[ATP]_m}\right)}{\left(1 + \dfrac{0.05\times[ATP]_i}{0.45\times[ADP]_i}e\left(\dfrac{-hF.\Delta\Psi}{RT}\right)\right)\left(1 + \dfrac{0.45\times 0.8\times[ADP]_m}{0.05\times[ATP]_m}\right)} \tag{35}$$

TABLE 3 Model parameters: TCA cycle

Symbol	Value	Units	Description	Eq.	Ref.*
k_{cat}^{CS}	3.2	s^{-1}	Catalytic constant of CS	13	*a*
E_T^{CS}	0.4	mM	Concentration of CS	13	*b*
K_M^{AcCoA}	1.26 10^{-2}	mM	Michaelis constant for AcCoA	13	*a*
K_M^{OAA}	6.4 10^{-4}	mM	Michaelis constant for OAA	13	*a*
C_{Kint}	1.0	mM	Sum of TCA cycle intermediates' concentration	14	*c*
k_f^{ACO}	12.5	s^{-1}	Forward rate constant of ACO	15	*a*
K_E^{ACO}	2.22		Equilibrium constant of ACO	15	*a*
k_{cat}^{IDH}	1.94–16.3	s^{-1}	Rate constant of IDH	16	*a*
E_T^{IDH}	0.109	mM	Concentration of IDH	16	*b*
$K_{i,NADH}$	0.19	mM	Inhibition constant by NADH	16	*a*
K_{ADP}^{a}	6.2 10^{-2}	mM	Activation constant by ADP	16	*a*
$[H^+]$	2.5 10^{-5}	mM	Matrix proton concentration	16	*k*
$k_{h,1}$	8.1 10^{-5}	mM	Ionization constant of IDH	16	*a*
$k_{h,2}$	5.98 10^{-5}	mM	Ionization constant of IDH	16	*a*
K_M^{ISOC}	1.52	mM	Michaelis constant for isocitrate	16	*a*
K_M^{NAD}	0.923	mM	Michaelis constant for NAD^+	16	*a*
K_{Ca}^{a}	0.00141	mM	Activation constant for Ca^{2+}	16	*a*
k_{cat}^{KGDH}	0.15–5.0	s^{-1}	Rate constant of KGDH	17	*a*
E_T^{KGDH}	0.5	mM	Concentration of KGDH	17	*f*
$K_M^{\alpha KG}$	1.94	mM	Michaelis constant for αKG	17	*a*
K_M^{NAD}	38.7	mM	Michaelis constant for NAD	17	*a*
$K_D^{Mg^{2+}}$	0.0308	mM	Activation constant for Mg^{2+}	17	*a*
$K_D^{Ca^{2+}}$	1.27 10^{-3}	mM	Activation constant for Ca^{2+}	17	*a*
$n_{\alpha KG}$	1.2		Hill coefficient of KGDH for αKG	17	*f*
Mg^{2+}	0.4	mM	Mg^{2+} concentration in mitochondria	17	*d*
k_f^{SL}	0.127	$mM^{-1}\ s^{-1}$	Forward rate constant of SL	18	*f*
K_E^{SL}	3.115		Equilibrium constant of the SL reaction	18	*a*
[CoA]	0.02	mM	Coenzyme A concentration	18	*b*
k_{cat}^{SDH}	1.0	s^{-1}	Rate constant of SDH	19	*f*
E_T^{SDH}	0.5	mM	SDH enzyme concentration	19	*f*
K_M^{Suc}	3.0 10^{-2}	mM	Michaelis constant for succinate	19	*e*
K_i^{FUM}	1.3	mM	Inhibition constant by fumarate	19	*e*
K_i^{Oaa}	0.15	mM	Inhibition constant by oxalacetate	19	*e*
k_f^{FH}	0.83	s^{-1}	Forward rate constant for FH	20	*a*
K_E^{FH}	1.0		Equilibrium constant of FH	20	*a*
k_{h1}	1.1310^{-5}	mM	Ionization constant of MDH	22	*j*
k_{h2}	26.7	mM	Ionization constant of MDH	22	*a*
k_{h3}	6.68 10^{-9}	mM	Ionization constant of MDH	23	*j*
k_{h4}	5.62 10^{-6}	mM	Ionization constant of MDH	23	*j*
k_{offset}	3.99 10^{-2}		pH-independent term in the pH activation factor of MDH	22	*a*
k_{cat}^{MDH}	2.775 10^{1}	s^{-1}	Rate constant of MDH	21	*f*
E_T^{MDH}	0.154	mM	Total MDH enzyme concentration	21	*b*
K_M^{MAL}	1.493	mM	Michaelis constant for malate	21	*a*
K_i^{OAA}	3.1 10^{-3}	mM	Inhibition constant for oxalacetate	21	*a*
K_M^{NAD}	0.2244	mM	Michaelis constant for NAD^+	21	*a*
K_f^{AAT}	0.644	s^{-1}	Forward rate constant of AAT	24	*a*
K_E^{AAT}	6.6		Equilibrium constant of AAT	24	*a*
K_{C_ASP}	0.01	s^{-1}	First order rate constant of aspartate consumption	25	*f*
Model parameters: oxidative phosphorylation					
r_a	6.394 10^{-10}	s^{-1}	Sum of products of rate constants	26,27	*g,h*
r_b	1.762 10^{-13}	s^{-1}	Sum of products of rate constants	27	*g,h*
1					*Continued*

TABLE 3 Continued

Symbol	Value	Units	Description	Eq.	Ref.*
r_{c1}	$2.656\ 10^{-19}$	s^{-1}	Sum of products of rate constants	26	*g,h*
r_{c2}	$8.632\ 10^{-27}$	s^{-1}	Sum of products of rate constants	26	*g,h*
r_1	$2.077\ 10^{-18}$		Sum of products of rate constants	26,27	*g,h*
r_2	$1.728\ 10^{-9}$		Sum of products of rate constants	26,27	*g,h*
r_3	$1.059\ 10^{-26}$		Sum of products of rate constants	26,27	*g,h*
ρ^{res}	0.0006–0.05	mM	Concentration of electron carriers (respiratory complexes I-III-IV)	26,27	*g,h*
K_{res}	$1.35\ 10^{18}$		Equilibrium constant of respiration	28	*g,h*
$\rho^{res(F)}$	0.0045	mM	Concentration of electron carriers (respiratory complexes II-III-IV)		
$\Delta\Psi_B$	0.05	*V*	Phase boundary potential	26,27,31	*g,h*
g	0.85		Correction factor for voltage	26,27	*g,h*
$K_{res(F)}$	$5.765\ 10^{13}$		Equilibrium constant of $FADH_2$ oxidation	29	
[FADH2]	1.24	mM	Concentration of $FADH_2$ (reduced)	29	
[FAD]	0.01	mM	Concentration of FAD (oxidized)	29	
p_a	$1.656\ 10^{-5}$	s^{-1}	Sum of products of rate constants	31,32	*g,h*
p_b	$3.373\ 10^{-7}$	s^{-1}	Sum of products of rate constants	32	*g,h*
p_{c1}	$9.651\ 10^{-14}$	s^{-1}	Sum of products of rate constants	31	*g,h*
p_{c2}	$4.585\ 10^{-14}$	s^{-1}	Sum of products of rate constants	31	*g,h*
p_1	$1.346\ 10^{-8}$		Sum of products of rate constants	31,32	*g,h*
p_2	$7.739\ 10^{-7}$		Sum of products of rate constants	31,32	*g,h*
p_3	$6.65\ 10^{-15}$		Sum of products of rate constants	31,32	*g,h*
ρ^{F1}	0.06–1.8	mM	Concentration of F_1F_0-ATPase	31,32	*g,h*
K_{F1}	$1.71\ 10^{6}$		Equilibrium constant of ATP hydrolysis	33	*g,h*
R	8.315	$V\ C\ mol^{-1}\ °K^{-1}$	Gas constant		
T	310.16	°K	Mammalian body temperature		
F	96480	$C\ mol^{-1}$	Faraday constant		
P_i	20.0	mM	Inorganic phosphate concentration	33	*i*
C_m	15.0	mM	Total sum of mito adenine nucleotides	34	*d*
V_{maxANT}	0.05–24.0	$mM\ s^{-1}$	Maximal rate of the ANT	35	*g,h*
h	0.5		Fraction of $\Delta\Psi_m$	35	*g,h*
$[ADP]_i$	0.05–0.2	mM	Cytoplasmic ADPi concentration	35	
$[ATP]_i$	6.5	mM	Cytoplasmic ATPi concentration	35	*d*
g_H	0.01	$mM\ s^{-1}\ V^{-1}$	Ionic conductance of the inner membrane	36	*g,h*
ΔpH	−0.6	pH units	pH gradient across the inner membrane	37	*k*
C_{PN}	10.0	mM	Total sum of mito pyridine nucleotides	30	*b*
C_{mito}	1.812	$mM\ V^{-1}$	Inner membrane capacitance	2	*l,m*
Model parameters: calcium dynamics					
V_{max}^{uni}	0.625–1.25	$\mu M\ s^{-1}$	V_{max} uniport Ca^{2+} transport	38	*g,h*
$[Ca^{2+}]_i$	$2.0\ 10^{-2}$–1.2	μM	Cytosolic Ca^{2+} concentration	38	*i*
$\Delta\Psi°$	0.091	Volts	Offset membrane potential	38	*g,h*
K_{act}	$3.8\ 10^{-4}$	mM	Activation constant	38	*g,h*
K_{trans}	0.019	mM	K_d for translocated Ca^{2+}	38	*g,h*
L	110.0		Keq for conformational transitions in uniporter	38	*g,h*
n_a	2.8		Uniporter activation cooperativity	38	*g,h*
V_{max}^{NaCa}	0.005–0.2	$mM\ s^{-1}$	V_{max} of Na^+/Ca^{2+} antiporter	39	*g,h*
b	0.5		$\Delta\Psi_m$ dependence of Na^+/Ca^{2+} antiporter	39	*g,h*
K_{Na}	9.4	mM	Antiporter Na^+ constant	39	*g,h*
$[Na^+]_i$	10.0	mM	Cytosolic Na^+ concentration	39	*g,h*
K_{Ca}	$3.75\ 10^{-4}$	mM	Antiporter Ca^{2+} constant	39	*g,h*
n	3		Na^+/Ca^{2+} antiporter cooperativity	39	*g,h*
f	0.0003		Fraction of free $[Ca^{2+}]_m$	12	*g,h*

*References: *a*, Dudycha et al., 2000; *b*, Albe et al., 1990; *c*, calculated from Jeffrey et al., 1999; *d*, Corkey et al., 1986; *e*, Singer, 1966; *f*, adjusted; *g*, Magnus and Keizer, 1997; *h*, Magnus, 1995; *i*, Crompton, 1999; *j*, calculated from data of Emyanitoff and Kelly, 1982; *k*, Jung et al., 1989; *l*, Gunter and Pfeiffer, 1990; *m*, Wojtczak et al., 1986.

The numbers (i.e., 0.45, 0.05, and 0.8) preceding $[ATP]_{i,m}$ and $[ADP]_{i,m}$ account for the nucleotides concentration in the correct ionization form that bind to their site in the ANT. An explicit expression of this equation, in terms of the ionic species participating in the translocation, is available in Magnus and Keizer (1997; see their Eq. 16 and Table 4).

The parameter h accounts for the fraction of $\Delta\Psi_m$ responsible for the large increase in the Michaelis-Menten constant for ATP uptake by energized mitochondria (Magnus and Keizer, 1997). The maximum rate for ADPi:ADPm exchange in the absence of ATP is given by V_{maxANT}.

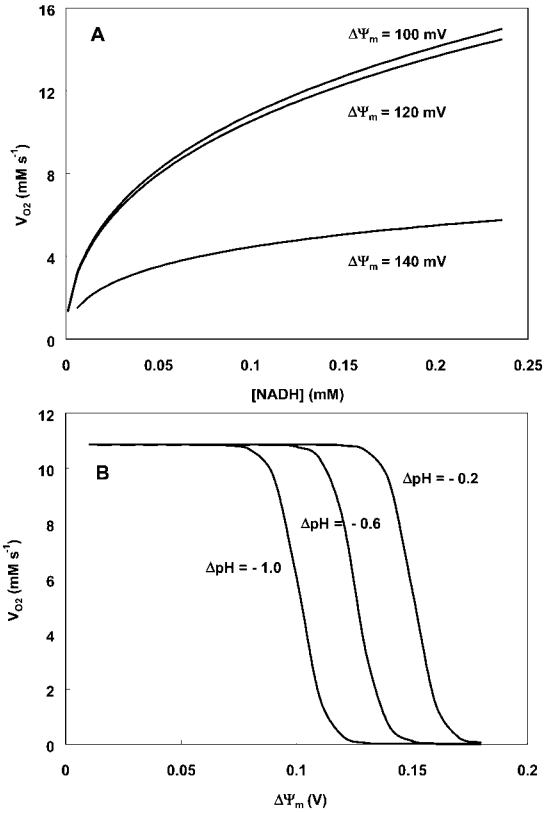

FIGURE A5 Dependence of the respiration rate, V_{O_2}, on redox potential, $\Delta\Psi_m$ and ΔpH. The respiration rate is studied as a function of: (*A*) NADH concentration in the mitochondrial matrix with $\Delta pH = -0.4$; $\rho^{res} = 1.2\ 10^{-2}$ mM; and $\Delta\Psi_m$ as indicated next to each curve (see Eq. 26); (*B*) $\Delta\Psi_m$ at various ΔpH values as indicated and fixed NADH concentration (=0.1 mM). The other parameter values in Eq. 26 are as indicated in Table 3.

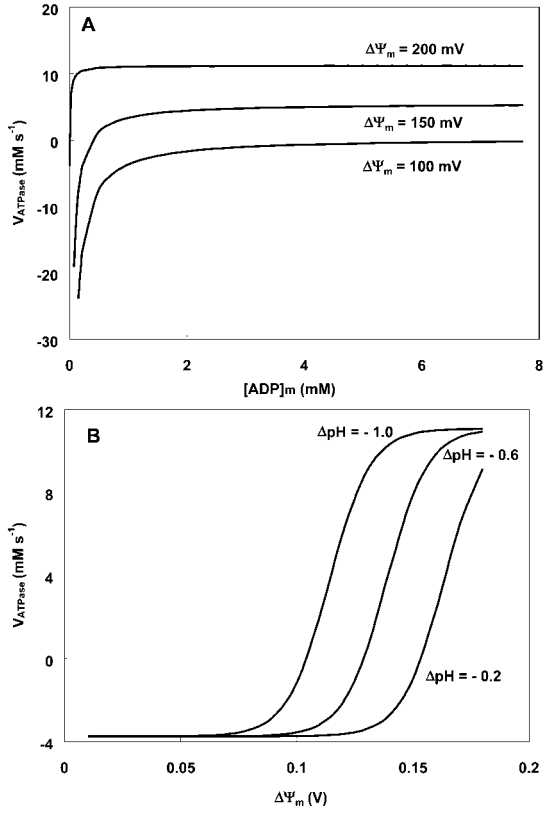

FIGURE A6 Dependence of F_1F_0-ATP synthase activity on ADP_m, $\Delta\Psi_m$ and ΔpH. The ATP synthetic (*positive*) or hydrolytic (*negative*) activity is plotted as a function of (*A*) ADP_m concentration with $\Delta pH = -0.4$, and $\rho^{F1} = 0.525$ mM, at different $\Delta\Psi_m$ as indicated (see Eq. 31); (*B*) $\Delta\Psi_m$ at the indicated ΔpH values and a constant $[ADP]_m$ (=1.0 mM).

The H^+ leakage is considered to be a linear function of the $\Delta\mu_H$ through a proportionality constant given by the H^+ conductance, g_H. Although the actual relationship is roughly exponential (Brown and Brand, 1986) there is an extensive linear region, especially at high $\Delta\Psi_m$ values, which justifies simplification of the rate equation, described as follows:

$$V_{Hleak} = g_H\,\Delta\mu_H \tag{36}$$

with

$$\Delta\mu_H = \frac{RT}{F}\Delta pH + \Delta\Psi_m. \tag{37}$$

The parameters of Eqs. 26–37 for this section of the model are described in the module: *Oxidative phosphorylation* in Table 3. Ordinary differential Eqs. 1–3 are the ones that can be assembled from this section (Table 1).

Mitochondrial calcium dynamics

The Ca^{2+} uniporter

The mitochondrial Ca^{2+} uniporter was modeled in Magnus and Keizer (1997) and depends on the electrochemical driving force for Ca^{2+}. Thus, $\Delta\Psi_m$ and cytoplasmic Ca^{2+} concentration ($[Ca^{2+}]_i$) are the primary determinants of the uniporter velocity as follows:

$$V_{uni} = V_{max}^{uni}\frac{\frac{[Ca^{2+}]_i}{K_{trans}}\left(1+\frac{[Ca^{2+}]_i}{K_{trans}}\right)^3\frac{2F(\Delta\Psi_m-\Delta\Psi^o)}{RT}}{\left(1+\frac{[Ca^{2+}]_i}{K_{trans}}\right)^4+\frac{L}{\left(1+\frac{[Ca^{2+}]_i}{K_{act}}\right)^{n_a}}\left(1-e^{\{-2F(\Delta\Psi_m-\Delta\Psi^o)/RT\}}\right)}. \tag{38}$$

This equation produces current-voltage curves that fit most available electrophysiological data (Wingrove et al., 1984; Gunter and Pfeiffer, 1990; Gunter and Gunter, 1994; see also electronic Appendix: http://www.jhmi.edu/bor/model.htm).

The Na^+/Ca^{2+} exchanger

The expression for the Na^+/Ca^{2+} antiporter was modified from Magnus and Keizer (1997). Available experimental evidence indicates that the antiporter is able to sense both $[Ca^{2+}]_m$ and $[Ca^{2+}]_i$ based on the reversal of its activity under pathological conditions (Griffiths et al., 1998). Under ischemic conditions the Na^+/Ca^{2+} antiporter may import Ca^2 while extruding Na^+. Extrusion of Ca^{2+} from the matrix is favored under normal conditions. Thus, our rate expression accounts for Na^+/Ca^{2+} antiporter dependence on the Ca^{2+} gradient across the inner mitochondrial membrane (Eq. 39).

$$V_{NaCa} = V_{max}^{NaCa}\frac{e^{\left(\frac{bF(\Delta\Psi_m-\Delta\Psi^o)}{RT}\right)}e^{\left(\ln\frac{[Ca^{2+}]_i}{[Ca^{2+}]_m}\right)}}{\left(1+\frac{K_{Na}}{[Na^+]_i}\right)^n\left(1+\frac{K_{Ca}}{[Ca^{2+}]_m}\right)} \tag{39}$$

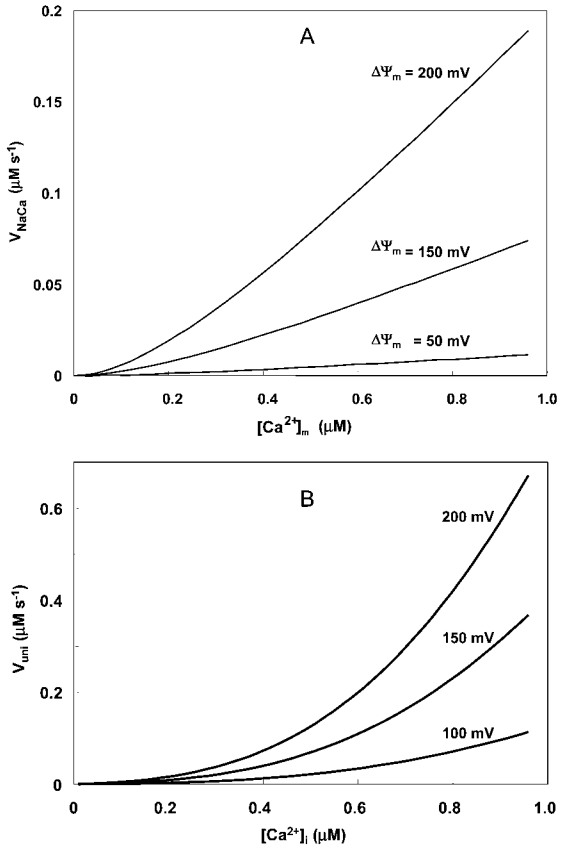

FIGURE A7 Rate of the mitochondrial Na^+/Ca^{2+} antiporter and Ca^{2+} uniporter. In *A* the rate of the Na^+/Ca^{2+} antiporter, V_{NaCa}, is analyzed for its dependence on $[Ca^{2+}]_m$ at different $\Delta\Psi_m$ with the following parameter values: $[Ca^{2+}]_i = 0.2\ \mu M$, $V_{max}^{NaCa} = 0.051$ mM s^{-1} (see Eq. 39). *B* shows the dependence of Ca^{2+} uniporter as a function of the $[Ca^{2+}]_i$ at various $\Delta\Psi_m$ with $V_{max}^{uni} = 0.0065$ mM s^{-1}. The remainder of the parameters involved in Eqs. 38 and 39 are described in Table 3.

The rate of the Na^+/Ca^{2+} antiporter, V_{NaCa}, displays an exponential behavior as a function of $[Ca^{2+}]_m$. As a result of the assumption of electrogenicity, V_{NaCa} exhibits a steeper dependence on $[Ca^{2+}]_m$ at high than at low $\Delta\Psi_m$ (Fig. A7, *A*).

The flux through the Ca^{2+} uniporter, V_{uni}, increases exponentially with $\Delta\Psi_m$ and the concentration of cytoplasmic Ca^{2+}, in the physiological range (Fig. A7, *B*). Clearly, the ability of the mitochondria for Ca^{2+} uptake increases with the energization of the inner membrane as reflected by $\Delta\Psi_m$.

Unit conversions

We have expressed all concentrations in millimolar (mM) units. For heart cells, the mitochondrial protein density is ~125 mg protein/ml (Randle and Tubbs, 1979). Because heart cells are compartmentalized into 58.5% and 36% cytosolic and mitochondrial volumes, respectively (Page, 1978; Katz, 1992) a factor of 0.125 converts measured nanomoles per milligram mitochondrial protein (nmol mg^{-1} protein) to mitochondrial mM terms.

Several of the parameters shown in Table 3 were taken from Magnus and Keizer (1997). We have converted their parameter values, usually expressed in nmol mg^{-1} protein, to mM by the conversion factor referred above.

GLOSSARY

$[ADP]_m$	Concentration of ADP in mitochondrial matrix
$[Ca^{2+}]_i$	Ca^{2+} concentration in cytosolic compartment
$[Ca^{2+}]_m$	Ca^{2+} concentration in mitochondrial matrix
[NADH]	Concentration of NADH in mitochondrial matrix
A_{F1}	Phosphorylation potential
A_{res}	Redox potential
αKG	α-ketoglutarate
ASP	Aspartate
CIT	Citric acid
F_1F_0-ATPase	Mitochondrial F_1F_0 ATP synthase activity
FUM	Fumarate
IDH	Isocitrate dehydrogenase
ISOC	Isocitrate
KGDH	α-ketoglutarate dehydrogenase
MAL	Malate
OAA	Oxalacetate
SCoA	Succinyl CoA
Suc	Succinate
TCA	Cycle tricarboxylic acid cycle
V_{AAT}	Rate of aspartate amino transferase
V_{ACO}	Rate of aconitase
V_{ANT}	Rate of the adenine nucleotide translocator (ANT)
V_{ATPase}	Rate of the F_1F_0 ATP synthase
V_{C_ASP}	Rate of Aspartate consumption
V_{CS}	Rate of citrate synthase
V_{FH}	Rate of fumarate hydratase
V_{He}	Rate of H transport across the membrane driven by NADH oxidation
$V_{He(F)}$	Rate of H transport across the membrane driven by $FADH_2$ oxidation
V_{Hleak}	H leak across the inner mitochondrial membrane
V_{Hu}	Rate of H uptake by mitochondrial via F1FoATPase
V_{IDH}	Rate of isocitrate dehydrogenase
V_{KGDH}	Rate of alpha ketoglutarate dehydrogenase
V_{MDH}	Rate of malate dehydrogenase
V_{NaCa}	Rate of the mitochondrial Na^+/Ca^{2+} antiporter
V_{O_2}	Rate of oxygen consumption
V_{SDH}	Rate of succinate dehydrogenase
V_{SL}	Rate of succinate lyase
V_{uni}	Rate of the Ca^{2+} uniporter in the mitochondrial membrane
$\Delta\Psi_m$	Electrical potential across the mitochondrial inner membrane
$\Delta\mu_H$	Proton motive force

SUPPLEMENTAL INFORMATION

An online Appendix of the Model of mitochondrial bioenergetics in cardiac myocytes can be found by visiting BJ online at http://www.biophysj.org.

The authors thank the collaboration of Minh N. Vo for assistance with the computational code.

Supported by National Institutes of Health grants R01HL54598 to Brian O'Rourke, R37H 36957 to Eduardo Marbán, and RO1 HL60133-01, P50 HL52307, The Whitaker Foundation, and the Falk Medical Trust to Raimond Winslow. Eduardo Marbán holds the Michael Mirowski, M.D. Professorship of Cardiology of the Johns Hopkins University.

REFERENCES

Ainscow, E. K., and M. D. Brand. 1999. Top-down control analysis of ATP turnover, glycolysis and oxidative phosphorylation in rat hepatocytes. *Eur. J. Biochem.* 263:671–685.

Albe, K. R., M. H. Butler, and B. E. Wright. 1990. Cellular concentrations of enzymes and their substrates. *J. Theor. Biol.* 143:163–195.

Baysal, K., D. W. Jung, K. K. Gunter, T. E. Gunter, and G. P. Brierley. 1994. Na^+-dependent Ca^{2+}efflux mechanism of heart mitochondria is not a passive $Ca^{2+}/2Na^+$ exchanger. *Am. J. Physiol.* 266:C800–C808.

Bohnensack, R. 1982. The role of the adenine nucleotide translocator in oxidative phosphorylation. A theoretical investigation on the basis of a comprehensive rate law of the translocator. *J. Bioenerg. Biomem.* 14:45–61.

Borutaite, V., V. Mildaziene, G. C. Brown, and M. D. Brand. 1995. Control and kinetic analysis of ischemia-damaged heart mitochondria: which parts of the oxidative phosphorylation system are affected by ischemia. *Biochim. Biophys. Acta.* 1272:154–158.

Brand, M. A., and A. Kesseler. 1995. Control analysis of energy metabolism in mitochondria. *Biochem. Soc. Trans.* 23:371–376.

Brandes, R., and D. M. Bers. 1997. Intracellular Ca^{2+} increases the mitochondrial NADH concentration during elevated work in intact cardiac muscle. *Circ. Res.* 80:82–87.

Brandes, R., and D. M. Bers. 2002. Simultaneous measurements of mitochondrial NADH and Ca^{2+} during increased work in intact rat heart trabeculae. *Biophys. J.* 83:587–604.

Brown, G. C., and M. D. Brand. 1986. Changes in permeability to protons and other cations at high proton motive force in rat liver mitochondria. *Biochem. J.* 234:75–81.

Brown, G. C., P. L. Lakin-Thomas, and M. D. Brand. 1990. Control of respiration and oxidative phosphorylation in isolated rat liver cells. *Eur. J. Biochem.* 192:355–362.

Chance, B., and G. R. Williams. 1956. The respiratory chain and oxidative phosphorylation. *Adv. Enzymol.* 17:65–134.

Chance, E. M., S. H. Seeholzer, K. Kobayashi, and J. R. Williamson. 1983. Mathematical analysis of isotope labeling in the citric acid cycle with applications to ^{13}C NMR studies in perfused rat hearts. *J. Biol. Chem.* 258:13785–13794.

Collins, T. J., P. Lipp, M. J. Berridge, and M. D. Bootman. 2001. Mitochondrial Ca^{2+} uptake depends on the spatial and temporal profile of cytosolic Ca^{2+} signals. *J. Biol. Chem.* 276:26411–26420.

Colomb, M. G., A. Chéruy, and P. V. Vignais. 1972. Nucleoside diphosphokinase from beef heart cytosol. I. Physical and kinetic properties. *Biochemistry.* 11:3370–3378.

Corkey, B. E., J. Duszynski, T. L. Rich, B. Matschinsky, and J. R. Williamson. 1986. Regulation of free and bound magnesium in rat hepatocytes and isolated mitochondria. *J. Biol. Chem.* 261:2567–2574.

Crompton, M. 1999. The mitochondrial permeability transition pore and its role in cell death. *Biochem. J.* 341:233–249.

Davey, G. P., and J. B. Clark. 1996. Threshold effects and control of oxidative phosphorylation in non-synaptic rat brain mitochondria. *J. Neurochem.* 66:1617–1624.

Duchen, M. R., A. Leyssens, and M. Crompton. 1998. Transient mitochondrial depolarizations reflect focal sarcoplasmic reticular calcium release in single rat cardiomyocytes. *J. Cell Biol.* 142:975–988.

Dudycha, S. 2000. A detailed model of the tricarboxylic acid cycle in heart cells. Johns Hopkins University. (Masters Dissertation.)

Elduque, A., A. Cortes, and J. Bozal. 1983. Kinetic mechanism of the molecular forms of chicken liver mitochondrial malate dehydrogenase. *Int. J. Biochem.* 15:539–545.

Emyanitoff, R. G., and P. J. Kelly. 1982. Kinetic characterization of mitochondrial malate dehydrogenase from *Dictyostelium discoideum*. *J. Gen. Microbiol.* 128:1767–1771.

Griffiths, E. J., C. J. Ocampo, J. S. Savage, G. A. Rutter, R. G. Hansford, M. D. Stern, and H. S. Silverman. 1998. Mitochondrial calcium transporting pathways during hypoxia and reoxygenation in single rat cardiomyocytes. *Cardiovasc. Res.* 39:423–433.

Groen, A. K., R. J. Wanders, H. V. Westerhoff, R. van der Meer, and J. M. Tager. 1982. Quantification of the contribution of various steps to the control of mitochondrial respiration. *J. Biol. Chem.* 257:2754–2757.

Gunter, T. E., and D. R. Pfeiffer. 1990. Mechanisms by which mitochondria transport calcium. *Am. J. Physiol.* 258:C755–C786.

Gunter, K. K., and T. E. Gunter. 1994. Transport of calcium by mitochondria. *J. Bioenerg. Biomemb.* 26:471–485.

Hafner, R. P., G. C. Brown, and M. D. Brand. 1990. Analysis of the control of respiration rate, phosphorylation rate, proton leak rate and proton motive force in isolated mitochondria using the 'top-down' approach of metabolic control theory. *Eur. J. Biochem.* 188:313–319.

Hansford, R. G., and D. Zorov. 1998. Role of mitochondrial calcium transport in the control of substrate oxidation. *Mol. Cell. Biochem.* 184:359–369.

Harris, D. A., and A. M. Das. 1991. Control of mitochondrial ATP synthesis in the heart. *Biochem. J.* 280:561–573.

Hatefi, Y., and D. L. Stiggall. 1976. Metal-containing flavoprotein dehydrogenases. *Meth. Enzymol.* XIII:222–255.

Heineman, F. W., and R. S. Balaban. 1990. Control of mitochondrial respiration in the heart in vivo. *Annu. Rev. Physiol.* 52:523–542.

Jafri, M. S., S. J. Dudycha, and B. O'Rourke.2001. Cardiac energy metabolism: models of cellular respiration. *Annu. Rev. Biomed. Eng.* 3:57–81.

Jeffrey, F. M., A. Reshetov, C. J. Storey, R. A. Carvalho, A. D. Sherry, and C. R. Malloy. 1999. Use of a single ^{13}C NMR resonance of glutamate for measuring oxygen consumption in tissue. *Am. J. Physiol.* 277:E1111–E1121.

Jung, D. W., M. H. Davis, and G. P. Brierley. 1989. Estimation of matrix pH in isolated heart mitochondria using a fluorescent probe. *Anal. Biochem.* 178:348–354.

Kadrmas, E. F., P. D. Ray, and D. O. Lambeth. 1991. Apparent ATP-linked succinate thiokinase activity and its relationship to nucleoside diphosphate kinase in mitochondrial matrix preparations from rabbit. *Biochim. Biophys. Acta.* 1074:339–346.

Katz, A. M. 1992. Structure of the heart and cardiac muscle. *In* Physiology of the Heart, 2nd Ed. Raven Press, Raven, New York.

Kohn, M. C., and D. Garfinkel. 1979. Computer simulation of metabolism in pyruvate-perfused rat heart. I. Model construction. *Am. J. Physiol.* 237:R153–R158.

Kohn, M. C., and D. Garfinkel. 1983. Computer simulation of metabolism in palmitate-perfused rat heart. I. Palmitate oxidation. *Ann. Biomed. Engin.* 11:361–384.

Korzeniewski, B. 1996. Simulation of oxidative phosphorylation in hepatocytes. *Biophys. Chem.* 58:215–224.

Korzeniewski, B. 1998. Regulation of ATP supply during muscle contraction: theoretical studies. *Biochem. J.* 330:1189–1195.

Magnus, G. 1995. A mitochondria-based model for bursting and its D-glucose dependence in the pancreatic beta cell. University of California, Davis. (PhD Dissertation.)

Magnus, G., and J. Keizer. 1997. Minimal model of β-cell mitochondrial Ca^{2+} handling. *Am. J. Physiol.* 273. *Cell Physiol.* 42:C717–C733.

McCormack, J. G., and R. M. Denton. 1984. Role of Ca^{2+} ions in the regulation of intramitochondrial metabolism in rat heart. Evidence from studies with isolated mitochondria that adrenaline activates the pyruvate dehydrogenase and 2-oxoglutarate dehydrogenase complexes by increasing the intramitochondrial concentration of Ca^{2+}. *Biochem. J.* 218:235–247.

McCormack, J. G., A. P. Halestrap, and R. M. Denton. 1990. Role of calcium ions in regulation of mammalian intramitochondrial metabolism. *Physiol. Rev.* 70:391–425.

Mitchell, P. 1961. Coupling of phosphorylation to electron and hydrogen transfer by a chemiosmotic type of mechanism. *Nature.* 191:144–148.

Mitchell, P. 1969. Chemiosmotic coupling and energy transduction. *In* Theoretical and Experimental Biophysics—A Series of Advances. A. Cole, editor. Dekker, New York. 159–216.

Miyata, H., H. S. Silverman, S. J. Sollott, E. G. Lakatta, M. D. Stern, and R. G. Hansford. 1991. Measurement of mitochondrial free Ca^{2+} concentration in living single rat cardiac myocytes. *Am. J. Physiol.* 261:H1123–H1134.

Murphy, M. P. 2001. How understanding the control of energy metabolism can help investigation of mitochondrial dysfunction, regulation and pharmacology. *Biochim. Biophys. Acta*. 1504:1–11.

Nichols, B. J., M. Rigoulet, and R. M. Denton. 1994. Comparison of the effects of Ca^{2+}, adenine nucleotides and pH on the kinetic properties of mitochondrial NAD(+)-isocitrate dehydrogenase from the yeast *Saccharomyces cerevisiae* and rat heart. *Biochem. J*. 303:461–465.

Page, E. 1978. Quantitative ultrastructural analysis in cardiac membrane physiology. *Am. J. Physiol*. 63:C147–C158.

Panov, A., and A. Scarpa. 1996. Independent modulation of the activity of alpha-ketoglutarate dehydrogenase complex by Ca^{2+} and Mg^{2+}. *Biochemistry*. 35:427–432.

Pietrobon, D., and S. R. Caplan. 1985. Flow-force relationships for a six-state proton pump model: intrinsic uncoupling, kinetic equivalence of input and output forces, and domain of approximate linearity. *Biochemistry*. 24:5764–5776.

Randle, P. J., and P. K. Tubbs. 1979. Carbohydrate and fatty acid metabolism. *In* Handbook of Physiology. R. M. Berne, N. Sperelakis, and R. Geiger, editors. American Physiological Society, Bethesda, Maryland. pp. 805–844.

Rizzuto, R., P. Pinton, W. Carrington, F. S. Fay, K. E. Fogarty, L. M. Lifshitz, R. A. Tuft, and T. Pozzan. 1998. Close contacts with the endoplasmic reticulum as determinants of mitochondrial Ca^{2+} responses. *Science*. 280:1763–1766.

Rossignol, R., M. Malgat, J. P. Mazat, and T. Letellier. 1999. Threshold effect and tissue specificity. Implication for mitochondrial cytopathies. *J. Biol. Chem*. 274:33426–33432.

Rutter, G. A., and R. M. Denton. 1988. Regulation of NAD^+-linked isocitrate dehydrogenase and 2-oxoglutarate dehydrogenase by Ca^{2+} ions within toluene-permeabilised rat heart mitochondria. Interactions with regulation by adenine nucleotides and NADH/NAD^+ ratios. *Biochem. J*. 252:181–189.

Saks, V., P. Dos Santos, F. N. Gellerich, and P. Diolez. 1998. Quantitative studies of enzyme-substrate compartmentation, functional coupling and metabolic channelling in muscle cells. *Mol. Cell. Biochem*. 184:291–307.

Saks, V. A., T. Kaambre, P. Sikk, M. Eimre, E. Orlova, K. Paju, A. Piirsoo, F. Appaix, L. Kay, V. Regitz-Zagrosek, E. Fleck, and E. Seppet. 2001. Intracellular energetic units in red muscle cells. *Biochem. J*. 356:643–657.

Shepherd, D., and P. B. Garland. 1969. The kinetic properties of citrate synthase from rat liver mitochondria. *Biochem. J*. 114:597–610.

Shiraishi, F., and M. A. Savageau. 1992. The tricarboxylic acid cycle in *Dictyostelium discoideum*. IV. Resolution of discrepancies between alternative methods of analysis. *J. Biol. Chem*. 267:22934–22943.

Singer, T. P., E. B. Kearney, and W. C. Kenney. 1973. Succinate dehydrogenase. *Adv. Enzymol. Rel. Ar. Mol. Biol*. 37:189–272.

Taylor, R. W., K. Birch-Machin, S. A. Bartlett, D. M. Lowerson, and D. M. Turnbull. 1994. The control of mitochondrial oxidations by complex III in rat muscle and liver mitochondria. *J. Biol. Chem*. 269:3523–3528.

Teipel, J. W., and R. L. Hill. 1971. The subunit interactions of fumarase. *J. Biol. Chem*. 246:4859–4865.

Territo, P. R., V. K. Mootha, S. A. French, and R. S. Balaban. 2000. Ca^{2+} activation of heart mitochondrial oxidative phosphorylation: role of the F0/F1-ATPase. *Am. J. Physiol. Cell Physiol*. 278:C423–C435.

Territo, P. R., S. A. French, and R. S. Balaban. 2001. Simulation of cardiac work transitions, in vitro: effects of simultaneous Ca^{2+} and ATPase additions on isolated porcine heart mitochondria. *Cell Calcium*. 30: 19–27.

Tran-Dinh, S., F. Beganton, T. T. Nguyen, F. Bouet, and M. Herve. 1996. Mathematical model for evaluating the Krebs cycle flux with non-constant glutamate-pool size by ^{13}C-NMR spectroscopy. Evidence for the existence of two types of Krebs cycles in cells. *Eur. J. Biochem*. 242:220–227.

Weiss, R. G., S. T. Gloth, R. Kalil-Filho, V. P. Chacko, M. D. Stern, and G. Gerstenblith. 1992. Indexing tricarboxylic acid cycle flux in intact hearts by carbon-13 nuclear magnetic resonance. *Circ. Res*. 70:392–408.

Weiss, R. G., R. Kalil-Filho, A. Herskowitz, V. P. Chacko, M. Litt, M. D. Stern, and G. Gerstenblith. 1993. Tricarboxylic acid cycle activity in postischemic rat hearts. *Circulation*. 87:270–282.

Williamson, J. R., C. Ford, J. Illingworth, and B. Safer. 1976. Coordination of citric acid cycle activity with electron transport flux. *Circ. Res*. 38:I-39–I-51.

Wingrove, D., J. Amatruda, and T. Gunter. 1984. Glucagon effects on the membrane potential and calcium uptake rate of rat liver mitochondria. *J. Biol. Chem*. 259:9390–9394.

Wojtczak, L., A. Żołkiweska, and J. Duszýnski.1986. Energy-storage capacity of the mitochondrial proton-motive force. *Biochim. Biophys. Acta*. 851:313–321.

Wright, B. E., M. H. Butler, and K. R. Albe. 1992. Systems analysis of the tricarboxylic acid cycle in Dictyostelium discoideum. I. The basis for model construction. *J. Biol. Chem*. 267:3101–3105.

Yu, X., N. M. Alpert, and E. D. Lewandowski. 1997. Modeling enrichment kinetics from dynamic 13C-NMR spectra: theoretical analysis and practical considerations. *Am. J. Physiol*. 272:C2037–C2048.